Aalto University
School of Electrical Engineering
Department of Radio Science and Engineering

Caner Demirpolat

X-band Interferometric Radar for Mapping Temporal Variability in Forest

Thesis submitted in partial fulfillment of the requirements for the degree of Master of Science in Technology.

Espoo 30.11.2012

Thesis supervisor: Prof. Martti Hallikainen
Aalto University

Thesis instructor: M. Sc. Jaan Praks
Aalto University

Aalto University
School of Electrical Engineering **Abstract of Master's Thesis**

Author: Caner Demirpolat

Name of the Thesis: X-band Interferometric Radar for Mapping Temporal Variability in Forest

Date: 30.11.2012 **Language:** English **Number of pages:** 9 + 86

School: School of Electrical Engineering

Department: Department of Radio Science and Engineering

Professorship: Space Technology **Code:** S.92

Supervisor: Prof. Martti Hallikainen, Aalto University

Instructor: M. Sc. Jaan Praks, Aalto University

Valuation, management and monitoring forest sources are crucial in today's world economically and ecologically. Remote sensing provides the possibility to map the extent, state and spatial structure of the forest and to detect and monitor the changes at lower cost than conventional land surveys. Spaceborne SAR has the advantage of acquiring images on a global scale in all weather conditions and independently of sunlight; therefore it has become a powerful tool in forestry applications.

In this thesis, five sets of dual-polarimetric (HH/VV) TanDEM-X coregistered single-look slant-range products, acquired between September 4 and November 9, 2011, are processed. For each TanDEM-X/TerraSAR-X pair, the canopy height models (CHM) are derived from the interferometric coherence phase using the LIDAR Digital Terrain model as auxiliary data. Using the land cover CLC2006 data, temporal variations in coherence statistics, average SPC heights, penetration depths and relative location of SPC to treetop are mapped with respect to coniferous, deciduous and mixed forest classes.

Results reveal that all parameters have certain dependencies on the forest class. Except coherence amplitude statistics, all parameters show sensitivity to the time of autumn and also to the SAR system polarization. Highest temporal variations are observed for deciduous forest, while coniferous forest seem to be least affected. Also, HH polarization is found to have stronger temporal variability than VV polarization for all forest classes.

Keywords: SAR, Forest, SPC, interferometry, coherence, penetration, polarization

Acknowledgements

This Master Thesis has been completed for the Department of Radio Science and Engineering, School of Electrical Engineering of Aalto University in February 2012-October 2012.

I would like to thank my supervisor, Prof. Martti Hallikainen, for providing me the opportunity to work on this thesis and his valuable comments for finalizing the work. I would like to express my deep gratitude to my instructor Jaan Praks for teaching, helping, guiding, motivating and inspiring me at every stage of my research and also generously sharing his previous work with me.

I would like to thank the Scientific and Technological Research Council of Turkey (TUBITAK) for awarding me with the scholarship for pursuing my M.Sc. degree in Aalto University, Finland. I would not be able to even start my studies without their financial support.

I am grateful to Daniel Molina Hurtado, Oleg Antropov, Jesus Llorente Santos and Melih Kandemir for helping me with the coding and other technicalities, also sharing their inspirational ideas about expanding my work.

I am thankful to all my friends, especially the ones that I have shared all amazing experiences in Finland. Burak Kaan Boyaci, Aydin Karaer, Melih Kandemir, Utku Ozturk, Fatos Ozen, Jesus Llorente Santos, Gorkem Cakmak, Petri Leppäaho, Sinan Kufeoglu, Can Cengiz, Suleyman Yilmaz, Emre Ilke Cosar, Vaida Vaitakunaite, Javier Tresaco, Alejandra Gomendio, Ankit Taparia, Usman Tahir Virk, Mohammad Arif Saber, Mazidul Islam have all impressed me with their generosity in friendship.

Finally, my special thanks go to my family, for their endless and unconditional love.

Espoo, November 30, 2012

Caner Demirpolat

Table of Contents

List of Figures

List of Tables

List of Acronyms

3D	Three-dimensional
AGB	Above Ground Biomass
ALS	Airborne Laser Scanning
ALTM	Airborne Laser Terrain Mapper
CHM	Canopy Height Model
CLC	CORINE Land Cover
CLC1990	First version of CLC Program
CLC2000	Update to the CLC1990
CLC2006	Update to the CLC2000
CLC25m	CLC Database in Raster Format
CoSSC	Coregistered Single look Slant range Complex
CORINE	Coordination of Information on the Environment
DEM	Digital Elevation Model
DLR	German Aerospace Center
DSM	Digital Surface Model
E	East
EADS	European Aeronautic Defence and Space
EEA	European Environment Agency
EM	Electromagnetic
ENVI	Environment for Visualizing Images
GmbH	Company with Limited Liability
GPS	Global Positioning System
H	Horizontal
HH	Horizontal Horizontal polarization
HV	Horizontal Vertical polarization
IDL	Interactive Data Language
IMAGE2000	Satellite image snap shot of the EU territory
InSAR	Interferometric Synthetic Aperture Radar
INU	Inertial Navigation Unit
ITP	Integrated TanDEM Processor
JRC	Joint Research Centre
LIDAR	Light Detection and Ranging
MCP	Mosaicking and Calibration Processor
N	North
NaN	Not-a-Number
PolInSAR	Polarimetric Interferometric Synthetic Aperture Radar
PRF	Pulse Repetition Frequency
RADAR	Radio Detection and Ranging
RAM	Random Access Memory
RMSE	Root Mean Square Error
RVoG	Random Volume over Ground
SAR	Synthetic Aperture Radar
SLAR	Side Looking Airborne Radar
SLR	Side Looking Radar
SNR	Signal-to-Noise Ratio

SPC	Scattering Phase Center
SSC	Single look Slant range Complex
SYKE	Finnish Environment Institute
TanDEM-X	TerraSAR-X add-on for Digital Elevation Measurement
TDX	TanDEM-X
TIFF	Tagged Image File Format
TSX	TerraSAR-X
V	Vertical
VH	Vertical Horizontal polarization
VV	Vertical Vertical polarization
UTM	Universal Transverse Mercator

List of Symbols

A_{eff}	antenna effective area
B	interferometric baseline
B_{eff}	effective baseline
B_n	perpendicular baseline
B_p	parallel baseline
c	speed of light
C	complex interferometric coherence
f	frequency
fe	flat earth removing phase
G_r	receiver antenna gain
G_t	transmitter antenna gain
h	scatterer height
h_{dtm}	original lidar DTM
h_{int}	height unknown in phase unwrapping
H	SAR satellite elevation
I_1	complex SAR image (master)
I_2	complex SAR image (slave)
K	hermitian product
k_z	vertical wavenumber
P_r	total received power
P_t	transmitter antenna peak amplitude power
q_s	displacement between resolution cells
R	range distance
S	power density
S_r	power density at receiver antenna
φ_{noise}	phase noise
φ_{ground}	measured ground phase of open areas
φ_{int}	phase unknown in phase unwrapping
φ_w	wrapped phase of lidar DTM
θ_i	incidence angle
$\Delta\theta_i$	incidence angle difference
$\Delta\eta$	coherent terrain displacement
$\Delta\beta$	changes in atmospheric path
$\Delta\varphi$	interferometric phase variation
ΔR	topography related phase difference
Δz	slant range difference
σ	radar cross section
Ψ	baseline angle with respect to local vertical
β	baseline angle with respect to local horizontal
λ	wavelength

1. Introduction

Due to the capability of acquiring high-resolution radar images independently of weather conditions and day-night cycle, spaceborne and airborne Synthetic Aperture Radar (SAR) systems have been effectively used in numerous Earth observation applications more than thirty years. Military applications such as targeting, surveillance and exploration; environmental monitoring of polar ice, glacier, ocean currents, oil spill, vegetation, soil, floods; and coherent applications such as change detection and elevation modeling have been the main SAR applications. Remote sensing of forest is economically significant for today's world and also becoming more significant due to the acceleration in climate and ecosystem changes. In forestry, most SAR studies focus on retrieving forest parameters related to the 3D structure such as tree height, biomass, vertical and horizontal heterogeneity as well as the intrinsic properties such as tree type, moisture content and leaf area index from the observed quantities such as backscattering coefficient and scattering phase center height.

For sustainable planning of forest resources, monitoring the exchange of matter between the landscape and atmosphere and the energy flow in ecosystems, forest biomass estimation is necessary and one of the most commonly studied problems of SAR remote sensing. Above-ground biomass (AGB) and stem volume are closely related parameters which can be estimated from observed SAR signatures such as backscatter [1], [2] and interferometric SAR coherence [3]. Forest height retrieval is another problem which has been one of the main focuses of SAR remote sensing since it is possible to relate forest biomass to the forest height by allometric equations [4], [5]. It has been demonstrated that tree heights that are retrieved by single baseline polarimetric interferometric SAR (PolInSAR) [6], or multibaseline PolInSAR [7], [8] can be used in biomass estimation. If an external digital elevation model is available, X-band single-pol interferometric coherence can also be used to retrieve the forest heights by Random Volume over Ground (RVoG) inversion model [9] - [13].

In addition to the research related to biomass and tree heights, SAR is now becoming more popular in land classification applications and land cover change analysis. It has been demonstrated that using different sets of polarimetric features, high accuracies in land classification can be achieved [14] - [16]. Temporal variations on the other hand, provide specific information related to land cover changes such as deforestation [17], [18]. So far, research of the SAR remote sensing in forestry has concentrated mainly on these domains.

1.1 Background and Motivation

Research on temporal variations of SAR signatures has mostly focused on SAR interferometric coherence [19] or backscattering coefficients [20] – [23]. In [19] and [20], the analysis was done with respect to land cover including tree species. However, the configuration of the SAR systems were all repeat-pass which was greatly affected by temporal decorrelation. The recently launched TanDEM-X mission provides the first single-pass polarimetric interferometric radar data acquired from space, as time series, without the effect of temporal decorrelation. Therefore seasonal, monthly or even shorter term variations in SAR signatures which are strongly dependent on scattering mechanisms can be observed in a global scale.

SAR scattering phase center (SPC) is a theoretical approximation of the average of all scattering objects in a scattering volume. SAR penetration depth is a measure of how deep incident SAR signal penetrates into a medium. In literature, SAR SPC location and penetration depth are parameters which are not completely studied for vegetation. Those parameters are to be expected to vary with respect to forest type and also leaf-on and leaf-off conditions. In simulations [24], penetration depth into coniferous type is found to be bigger than deciduous type for a stand with the same tree number and heights; however no extensive study of aforementioned parameters and their temporal variability on real SAR data has been published. Thus, the thesis aims to introduce an analysis of those coherent SAR signatures with respect to forest type and time during autumn. Results are expected to contribute to the evaluation of the success of TanDEM-X mission in forest monitoring and also provide potentially distinctive

information about forest types, especially for scientists who are interested in land cover classification. Even though the land classification accuracies were found to be high for land cover classes using full-polarimetric data, the classification accuracy for tree species was not that high [14], [15].

1.2 Research Problems

This thesis mainly concentrates on six problems. The first is the dependencies of interferometric coherence, SPC height and SPC-related statistics (mean penetration and the location of SPC relative to treetop) on the forest classes. The second is the possibility and potential of observing temporal variations in those statistics with spaceborne X-band interferometric radar. The third problem implies how the instant statistics and the temporal variations of those are related to the Julian date. Dependencies of the temporal variations on forest type constitute the fourth problem. The fifth problem investigates the relationship between variability in coherence amplitude statistics and variability in SPC and SPC-related statistics. The final problem is to seek to answer the question what the influences of SAR system polarization (VV or HH) are on the statistics and the variations.

1.3 Thesis Structure

The thesis is organized in six chapters. In Chapter 1, a general background, motivation, research goals and the structure of the thesis are presented. Chapter 2 gives an overview of RADAR theory, backscattering, general SAR system properties, and terrain height measurement by SAR and describes the parameters affecting SAR interferometric coherence and phase. Chapter 3 presents the data that have been used in the thesis. Chapter 4 describes the methodology followed, mainly the steps of interferometric processing and retrieval of the parameters of interest. Chapter 5

presents and discusses the results of the research. Chapter 6 discusses the conclusions of this study and makes recommendations for future work.

2. Overview of Interferometric SAR

In this chapter, an overview of the theoretical background is given. The terms, equations and expressions are introduced here which are going to be used in the following chapters. Section 2.1 gives an overview of radar, Section 2.2 explains the radar backscattering phenomenon and mechanisms, and finally Section 2.3 describes the SAR system formation and interferometric SAR technique of terrain altitude measurements.

2.1 Radar

Radar is an electromagnetic system that uses radio signals to detect and locate objects, and also extract other information from the echo signal. Radar systems operate in the microwave region of the electromagnetic spectrum which extends from wavelengths of about 1 mm (frequency 300 GHz) to around 1 m (frequency 300 MHz). Compared to passive sensors that rely on electromagnetic waves that have been produced by another source such as sunlight or thermal radiation; radar systems have their own transmitter. A radar transmitter transmits short bursts or pulses of EM radiation in the direction of interest and the radar receiver records the strength and the origin of the echoes or reflections. Usually radar systems require more complex hardware and higher power consumption that the passive microwave systems, however they can collect data independently of other radiation sources, such as Sun. Unlike optical sensors, microwave radar systems are not affected by cloud cover or mist, they usually operate independently of atmospheric conditions.

Radar systems may or may not produce images, they may be ground based, e.g. ships and air traffic towers, or they may be mounted on a spacecraft or aircraft. Airborne and spaceborne radar systems are mostly imaging radar systems and they employ an antenna fixed below the platform and directed to the side. Such systems are called side-looking radar (SLR) when mounted on a spacecraft or side-looking airborne

radar (SLAR) when mounted on an aircraft. Modern imaging radar systems use more advanced data processing methods and are referred as synthetic aperture radar (SAR).

If the radar transmitter antenna has a peak output power of P_t [W] and gain of G_t, the power density S [W/m^2] at a range distance R is given by:

$$S = \frac{P_t\, G_t}{4\,\pi\, R^2} \tag{3.1}$$

The total amount of energy intercepted by the target is proportional to the target's receiving area. Some of the incident energy is absorbed by the target and the rest is reflected. Reflected energy can have a certain pattern which may result in some gain towards the operating radar system. All these parameters are usually combined into a single parameter called radar cross-section (σ). When Equation 3.1 is combined with radar cross-section, the power density at the radar system's receiver is

$$S_r = \frac{P_t\, G_t\, \sigma}{(4\,\pi\, R^2)^2} \tag{3.2}$$

assuming the distance from target to the receiver antenna is also equal to R. The total received power P_r is found simply by multiplying the power density S_r with effective area A_{eff} [m^2] of the receiver antenna:

$$A_{eff} = \frac{G_r\, \lambda^2}{4\,\pi} \tag{3.3}$$

where G_r represents the gain of the receiving antenna and λ is the wavelength of the system. Finally,

$$P_r = \frac{P_t\, G_t\, G_r\, \sigma\, \lambda^2}{64\,\pi^3\, R^4} \tag{3.4}$$

The radar Equation 3.4 presented above is simplistic since it does not include the polarization effect and extra losses in the whole system.

Imaging radar systems operate at a specific frequency or wavelength. For remote sensing with SAR, the most commonly used frequency bands are X-band (8.0 – 12.5 GHz), C-band (4.0 – 8.0 GHz), S-band (2.0 – 4.0 GHz), L-band (1.0 – 2.0 GHz) and P

(0.3 – 1.0 GHz). In this thesis, only the SAR systems operating in X-band are considered [25] – [28].

2.2 Radar Backscattering

Backscatter or backscattering is the reflection of waves back to the incoming direction. All radars measure backscattered waves. The radar backscatter is significantly affected by both the system and target parameters. Frequency, antenna polarization and local incidence angle are considered as the system parameters; on the other hand, dielectric constant, surface roughness, the size, shape and orientation of the scatterers are counted as the target parameters. There are several scattering mechanisms. Two main types of scattering mechanisms are often distinguished: Surface and volume scattering which will be explained in the next subsection.

2.2.1 Scattering Mechanisms

Scattering mechanisms refer to the way radar signal is reflected from the target. Surface and volume scattering are significant scattering mechanisms to be understood for SAR remote sensing of forest. Surface scattering implies that the transmitted radar signal that has reached the terrain is reflected from a surface. The wave reflections from a side of building, water or open fields are all examples of surface scattering. Roughness (compared to wavelength) of the surface is one the most important factors that have a significant impact on the amplitude, phase and polarization of the signal reflected back to the receiver antenna. Smooth (compared to wavelength) surfaces tend to reflect the incoming signal into one direction; on the contrary, rough surfaces tend to reflect the signal into many different directions. Local incidence angle is another parameter that affects surface backscatter greatly. For smooth surfaces, incident angles less than 30° result in quasi-specular scattering and incident angles between 30° and 80° result in a dominating Bragg Scattering [27]. Also, incoming wave frequency has a considerable effect on the surface scattering. While frequency

goes lower, the wavelength gets longer and surfaces appear smoother, therefore leading to a dominant specular scattering.

Volume scattering refers to the way that the signal is not only reflected by the upper surface of the terrain but also by the surfaces along with elements below this surface canopy. Volume scattering is mostly apparent in soil and vegetation. Amount, shape, orientation of the scattering objects and their relative size to the wavelength has a great impact on the returned wave. Additionally, there exists another scattering mechanism called double bounce scattering which occurs when the incoming wave is reflected by two surfaces which are perpendicular or near perpendicular to each other.

In addition to parameters mentioned before, the dielectric constant of the scattering objects also affects the backscatter. High water content in the scattering objects leads to high dielectric constant and therefore results in higher reflection coefficient. Dry or frozen materials have usually lower backscatter power in comparison to wet materials [25], [26], [28].

2.2.2 Radar Signal Scattering from Forest

For typical remote sensing radar, volume scattering is most apparent in vegetated area and is also the dominant scattering mechanism. In vegetation, the return signal originates from multiple elements such as leaves, branches, trunks, bushes etc. The wavelength of the incident wave determines the dominant element which takes part in the scattering process. At L-band, main scattering elements are the branches and at C-band and X-band they are leaves, needles, twigs, etc. [26]. In the study [29], X-band backscatter is found to be decreased on removal of the leaves, while there was a slight decrease in C-band and no decrease in L-band and S-band.

Volume scatter in forest depends highly on the target properties as well as the radar system characteristics. Sizes of the leafs, branches, stalks, the density of foliage, height of the trees, presence of lower canopy vegetation, soil-ground conditions, moisture content all have significant effect on the whole process [28]. A dense canopy attenuates the incident wave gradually and reduces the energy reaching the ground. On the way back, the reflected wave is furthermore attenuated. Since water has relatively high dielectric constant, forest backscatter is expected to increase by the

both water content of the leaves and the soil. Therefore, backscatter in summer conditions are usually expected to be lower than winter conditions. For boreal forest, temperature is also a significant factor to be considered in the analysis since it directly affects the dielectric constant.

2.2.3 Scattering Phase Center

Volume scattering in vegetation implies that the incident signal is not directly reflected by top layer of the canopy but by a volume of canopy. Therefore total return signal can be considered as a coherent combination of many reflections. In radar systems, there exists a point which the return signal appears to be coming. This point is a theoretical approximation which represents the average of all scattering objects and called the scattering center. In case of InSAR systems, when the measurements are in units of interferometric phase, it is called scattering phase center.

From treetop to the ground, scattering phase center is at some point depending on the physical properties of the forest and acquisition system properties that have already been discussed in the subsections of Section 2.2. For instance, it is usually located near canopy top in dense forest, while it is about half of the canopy height in sparse forest [30]. Also higher system frequencies lead scattering phase center to move towards the canopy top since with a decreasing wavelength, the scattering objects are bigger in size and therefore resulting in more reflections from leaves, branches, etc.

2.3 Synthetic Aperture Radar Interferometry

In this section, a typical SAR system and basics of SAR interferometry are explained. First, the formation of synthetic aperture and SAR system properties are presented, then the fundamentals of SAR interferometry are discussed.

2.3.1 SAR System

SAR is a sidelooking radar system which synthesizes an extremely large antenna or aperture by taking samples looking sideways along a flight path which generates high-resolution imagery. A typical SAR system is mounted on a spacecraft or aircraft and carries radar with the antenna pointed to the Earth's surface in the plane perpendicular to the orbit. The target is repeatedly illuminated with pulses of radio waves by a beam-forming antenna called the transmitter antenna and the response returned to the receiver antenna or antennas at different positions are coherently detected, recorded and processed afterwards [31] – [33]. Figure 2.1 visualizes a typical SAR system.

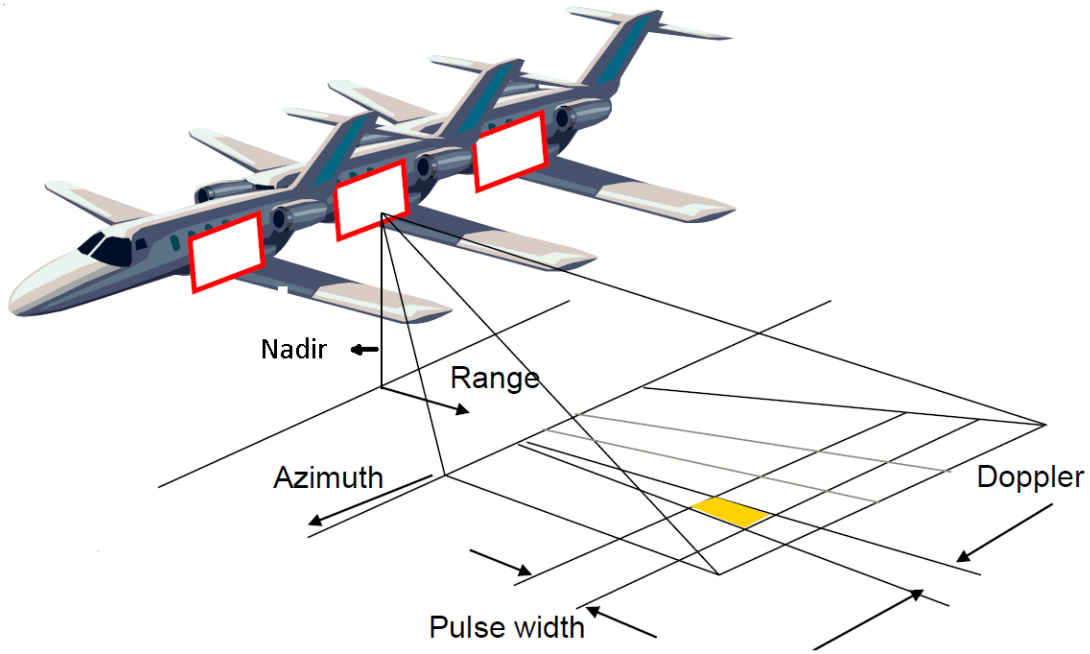

Figure 2.1 A typical SAR system. *Adopted from [33].*

The inclination of the antenna with respect to the nadir is known as the off-nadir angle and due to the curvature of the Earth; the incidence angle of the radiation is higher than the off-nadir angle. Azimuth is the term used for referring the linear distance in a parallel direction to the spacecraft's orbit. The term slant range is measured perpendicular to LOS and indicates the distance from the radar towards each target [34].

Polarization of the antennas is another important feature of the SAR system. It is possible theoretically to assign the transmitted signal one of the elliptical, circular or linear polarizations. However, in practice, SAR systems are assigned the linear polarizations of horizontal (H) or vertical (V) by the transmitter and receiver antennas. Therefore, the polarization of the SAR system is one of the possible combinations HH, VV, HV or VH where first letter represents the polarization of the transmitted signal and second letter indicates the polarization of the received signal. In this thesis, SAR systems with HH and VV polarization are considered and therefore the dataset acquired with the corresponding polarizations will be called HH-pol and VV-pol respectively [25], [28].

2.3.2 SAR Interferometry

SAR interferometry is an established technique for collection of topographic data. It is applied through the construction of an interferogram using two complex SAR images acquired from slightly different positions or times. These differences are known as spatial and temporal baseline respectively. Temporal baseline is introduced when the SAR images are acquired through exactly the same flight tracks at different times. The SAR data obtained on tracks of temporal baseline contain information about the changes in the observed scene such as coherent movement of the scatterers due to earthquakes, volcanic activity and landslides. Spatial baseline, on the other hand, is introduced when SAR images are acquired from slightly different flight paths simultaneously. The spatial baseline can be geometrically separated into parallel (B_p) and perpendicular (B_n) components also known as the effective baseline (B_{eff}). Figure 2.2 illustrates the geometry. B_{eff} is the most significant parameter in interferometric processing. In airborne systems, B_{eff} is usually in the range of a few meters up to several tens, however in spaceborne systems it can go up to a few kilometers [26], [28].

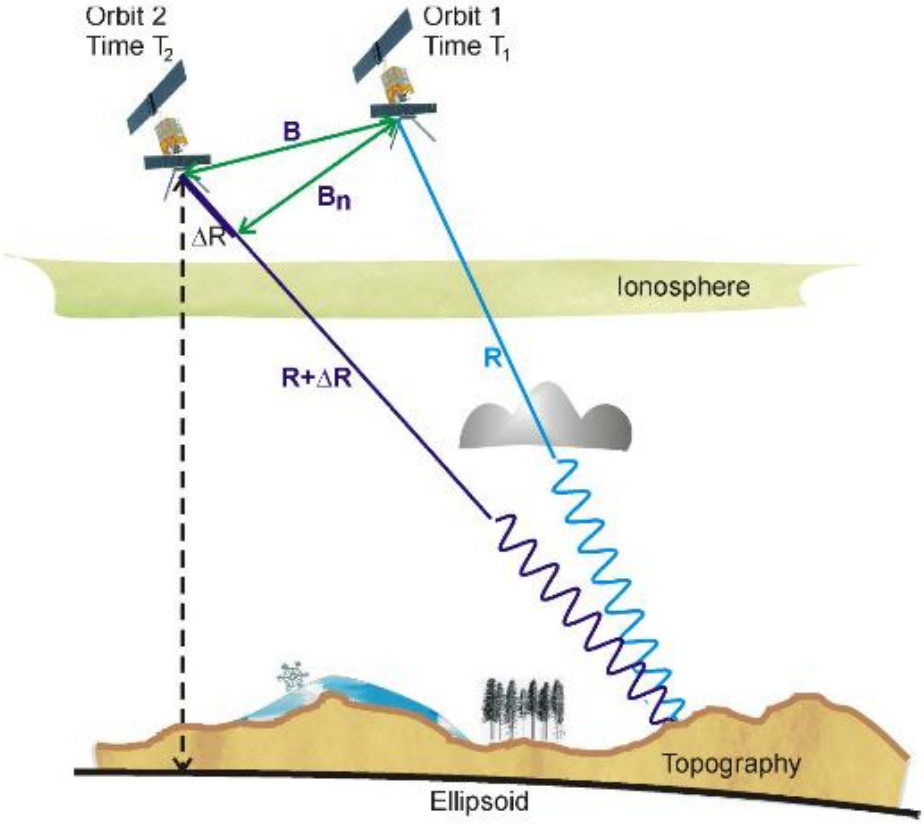

***Figure 2.2 Interferometric SAR formation**. The image is acquired from [35].*

There are several methods of collecting interferometric SAR data. In single-pass interferometry, two antennas are located on a single platform which is either airborne or spaceborne. One antenna works as a transmitter and receiver simultaneously, the other one works only as a receiver. In repeat-pass interferometry, a single antenna works as the transmitter and the receiver on a platform (spaceborne or airborne) which makes two or more passes over the region of interest.

2.3.3 Interferometric Coherence Magnitude

Interferogram of two complex SAR images I_1 and I_2 is generated by the construction of Hermitian product K of these two images which have to be already co-registered with sub-pixel accuracy:

$$K = < \begin{bmatrix} I_1 \\ I_2 \end{bmatrix} [conj(I_1)\ \ conj(I_2)] > = \begin{bmatrix} < I_1 * conj(I_1) > & < I_1 * conj(I_2) > \\ < I_2 * conj(I_1) > & < I_2 * conj(I_2) > \end{bmatrix} \tag{3.5}$$

Here $conj$ symbolizes the complex conjugation and <…> indicates the expected value. Coherence is a measure of the quality of the interferograms and defined as the absolute value of the normalized complex cross correlation between both images:

$$C = |C|\, e^{j\varphi} = \frac{|<I_1 * conj(I_2)>|}{\sqrt{<I_1 * conj(I_1)> * <I_2 * conj(I_2)>}} \tag{3.6}$$

Generally in literature, magnitude of the complex coherence is referred as coherence and in this study it is also referred the same way. Frequency-domain representation of fluctuations in the phase of a signal caused by time domain instabilities is referred as phase noise. In interferometric SAR systems, phase noise can be measured by means of the coherence. Coherence can take values from 0 up to 1 and, it is a measure of the phase noise. When coherence is equal to 1, it implies that the signal does not include any phase noise. Oppositely, when it is equal to 0, it means the signal is pure noise. For TanDEM-X mission, the observed interferometric coherence can be divided into several components [36], [37]:

$$|C| = |C|_{ambiguity} |C|_{azimuth} |C|_{quantization} |C|_{range} |C|_{temporal} |C|_{SNR} |C|_{volume} \tag{3.7}$$

The component $|C|_{ambiguity}$ refers to the decorrelation caused by distributed range and azimuth ambiguities. $|C|_{azimuth}$ stands for the azimuth spectral decorrelation caused by the relative shift of Doppler spectra while $|C|_{range}$ represents the range spectral decorrelation. $|C|_{quantization}$ is the decorrelation caused by the quantization of the recorded raw data signals. $|C|_{temporal}$ represents the temporal decorrelation that arises from the variations in geometry or the backscattering behavior of the scatterers between the times of acquisitions. For bistatic TanDEM-X acquisition mode, temporal decorrelation is not effective, thus can be completely neglected. However, [37] suggests that 3 seconds of temporal baseline is also effective in monostatic TanDEM-X acquisitions. The sixth term $|C|_{SNR}$ stands for the decorrelation due to limited Signal-to-Noise Ratio (SNR). Thermal noise in the receivers leads to a coherence loss [36] in the order of:

$$|C|_{SNR} = \frac{1}{\sqrt{((1+\mathrm{SNR}_1^{-1})*(1+\mathrm{SNR}_2^{-1}))}} \tag{3.8}$$

where SNR_1 is the SNR for interferometric channel 1 and SNR_2 is for channel 2. The last term $|C|_{volume}$ refers to the decorrelation caused by volume scattering in the target, e.g. in vegetated areas. After azimuth and range filtering, $|C|_{azimuth}$ and $|C|_{range}$ can be also neglected. Therefore, final interferometric coherence in our dataset can be expressed as:

$$|C|_{observed} = |C|_{ambiguity}|C|_{quantization}|C|_{SNR}|C|_{volume} \tag{3.9}$$

Only volume decorrelation is dependent on the target properties, thus other terms can be considered as the additional noise to the system. It is suggested that decorrelation $|C|_{ambiguity}|C|_{quantization}|C|_{SNR}$ can be recovered by the assumption that coherence over the bare surfaces should be equal to one [38]. However, this approach introduces a new parameter to the system and increase the number of unknowns traditional inversion scenarios, thus it is not applied in this study.

2.3.4 Altitude Measurement of Terrains by Interferometric Coherence Phase

The phase of the complex coherence is called the interferometric phase which can be formulated as

$$\varphi = \arctan\left(\frac{Im\{I_1 * Conj(I_2)\}}{Re\{I_1 * Conj(I_2)\}}\right) + 2\pi n \quad n = (\dots, -2, -1, 0, 1, 2, \dots) \tag{3.10}$$

Interferometric phase contains both the range and topography-dependent information and can also be decomposed into several terms as [28, 31, 39]:

$$\varphi = \frac{4\,\pi\,B_n}{\lambda\,R\,tan(\theta_i)}\Delta z + \frac{4\,\pi\,B_n}{\lambda\,R\,sin(\theta_i)}\Delta R + \frac{4\pi}{\lambda}\Delta\eta + \frac{4\pi}{\lambda}\Delta\beta + \Delta\varphi_{\mathrm{noise}} + 2\pi n \tag{3.11}$$

The first two terms above are related to the geometry of the SAR system by means of perpendicular baseline B_n, range R and incidence angle θ_i. Δz included in the first term is slant range difference which leads to the phase fringes which can be removed by flat-earth phase removal (see Subsection 4.1.5). In the second term, ΔR includes the topography related information, thus the most important parameter for producing DEM. Δɲ refers to the coherent terrain displacement and thus the third term is related to the coherent movement of all scatterers within the resolution cell in the time interval between two acquisitions caused by earthquakes, volcanic activity or ground subsidence etc. The fourth term expresses the changes in the atmospheric path Δβ such as electron density in ionosphere, water vapor etc. $\Delta\varphi_{\text{noise}}$ represents the effect of noise and 2πn is just the phase ambiguity later to be resolved by phase unwrapping [28].

The second term in Equation 3.11 includes topographic information by means of the following relations [40]:

Two SAR receivers separated by baseline B (oriented at an angle β with respect to local horizontal) are at elevation H. The ranges R and R+ΔR to the scatterer at the height h is measured independently at two receiver antennas (see Figure 2.3). Applying law of cosine, Equation 3.12 is obtained:

$$(R + \Delta R)^2 = R^2 + B^2 - 2BRcos(\Psi + \beta) \tag{3.12}$$

When Equation 3.12 is solved for depression angle Ψ, h is obtained as:

$$h = H - R\sin(\Psi) \tag{3.13}$$

The relationship between a variation in scatterer height δh and resulting variation in range to the two receivers $\delta(\Delta R)$ is derived using differentials:

$$\frac{dh}{d(\Delta R)} = \frac{dh}{d\Psi}\frac{d\Psi}{d(\Delta R)} = \frac{dh}{d\Psi}\frac{1}{d(\Delta R)/d\Psi} \tag{3.14}$$

From Equation 3.13,

$$\frac{dh}{d\Psi} = -R\cos(\Psi) \tag{3.15}$$

Assuming $R \gg B$ and $R \gg \Delta R$, Equation 3.12 becomes

$$\Delta R \approx -B\cos(\Psi + \beta) \tag{3.16}$$

which yields

$$\frac{d(\Delta R)}{d\Psi} \approx B\sin(\Psi + \beta) \tag{3.17}$$

Combining these equations leads to the formula

$$\frac{dh}{d(\Delta R)} \approx \frac{-R\cos(\Psi)}{B\sin(\Psi+\beta)} \tag{3.18}$$

and finally

$$|\,\delta h\,| \approx \frac{R\cos(\Psi)}{B\sin(\Psi+\beta)}\ |\,\delta(\Delta R)|\tag{3.19}$$

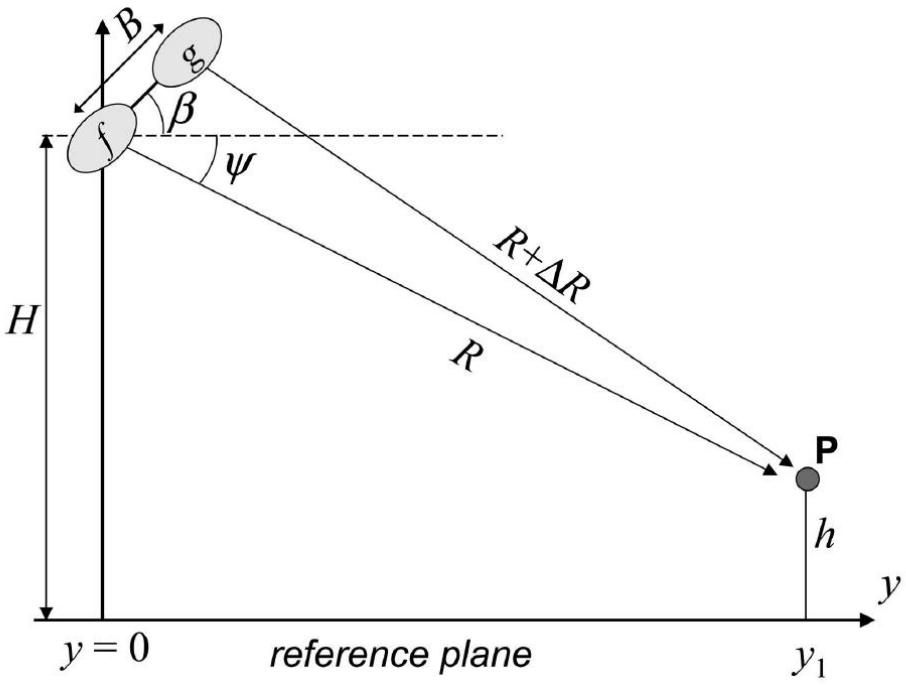

Figure 2.3 SAR imaging geometry for terrain altitude measurements. *Image is taken from [40].*

3. Test Site and the Data

In this chapter, test site and the data used in the thesis is introduced. Section 3.1 describes the geographical characteristics of the test site. Section 3.2 presents the information regarding the land cover database which is used for retrieving parameters of interest with respect to forest types. Also, a short history of how the database is produced is given. Section 3.3 presents the properties of SAR data and provides information about satellites and the mission wherein SAR data is collected. Section 3.4 focuses on the reference tree height and terrain measurements which are also used as auxiliary data. Finally, Section 3.5 presents the weather conditions during each SAR acquisition.

3.1 Test Site

The test site is located in the Kirkkonummi region of the southern Finland having the eastings from 352826 to 356715 [m] and northings from 6679551 to 6683440 [m] in UTM coordinates. In geographical coordinates, the region covers approximately N 60° 13’ - N 60° 15’ and E 24° 20’ - E 24° 25’. A Google-Earth image of the approximate test site can be seen in Figure 3.1.

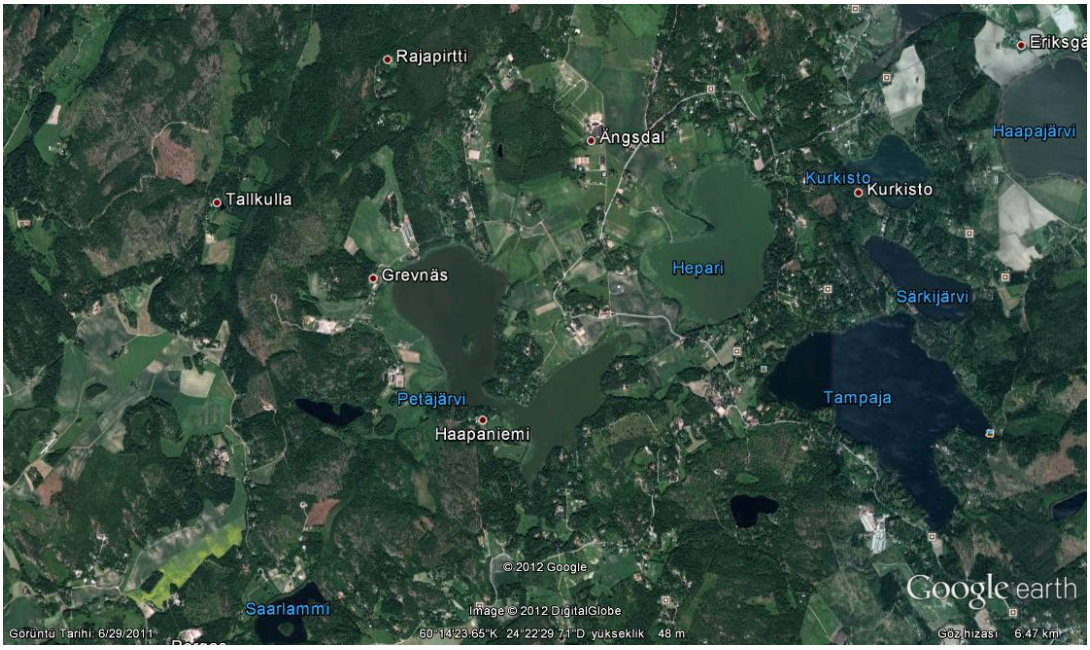

Figure 3.1 Optical image of the approximate test site. *Size of the region is about 7 km by 5 km. Image is adopted from [41].*

The test site is mainly formed by lakes, agricultural fields, forest, open areas and also small portions of urban areas and industrial regions. It is not flat, there are many small hills up to 60 meters and most forest grow on those. Forest in this site is heterogeneous and the dominant species of the forest are Scots pine, Norway spruce, birch and alder. Forest inventory information shows that the stem volume can go up to 250 m^3/ha with maximum tree heights less than 30 m [11].

3.2 Land Cover Data

In order to make the analysis of interferometric variables depending on the forest type, CLC2006 database has been used. CLC2006 database was an update to the previous project CLC2000, thus this section starts with a brief history of CLC Program, production process and the properties of the CLC2000 database, continues with how the update is conveyed.

The Coordination of Information on the Environment (CORINE) Programme was proposed in 1985 by the European Comission in order to gather information on priority topics about the environment such as land cover, coastal erosion, biotopes etc. The land cover component of the programme (CLC) contained geographical information on biophysical land cover. The initial version of the CLC, CLC1990 project has been completed around the end of 1990's. For the purpose of updating the CLC data, European Environment Agency (EEA) and Joint Research Centre (JRC) launched the CLC2000 and IMAGE2000 project. Finland did not participate CLC1990 project, however after Finnish Ministry of Environment signed the formal commitment in 2001, a new CLC2000 databases were produced for whole Finland by the Finnish Environment Institute (SYKE): the standard European CLC2000 and a more detailed version for national use. In 2005, EEA management board took a decision to update the CLC data in order to map the land cover changes between 2000 and 2006, therefore Corine Land Cover update (CLC2006) is released in 2006 [42].

Production of CLC2000 database of Finland was based on the automated interpretation of satellite images and data integration with existing digital map data. Map data provided the information about land use and soils, and satellite images were used to describe vegetation type and coverage as well as in updating the map data. The main outputs of the CLC2000 project in Finland were the national satellite image mosaic (national IMAGE2000), the national CLC2000 database in vector format and the Finnish CLC25m raster database. Finnish CLC25m had resolution of 25x25 m and the classification of the database followed CLC nomenclature. The database is delivered in TIFF format having the dimensions of 28800x49600. Every pixel in the image has an 8-bit integer value corresponding to each specific class. Out of 44 total CLC classes, 31 exist in Finland. According to the database, dominant forest types, their corresponding pixel values and their percentage over whole Finland are given in Table 3.1.

Table 3.1 Forest classes and their coverage over Finland in CLC2000 database. *Calculated pixel by pixel using the final product delivered: CLC25m. Sea, lakes, rivers, etc. are also included in calculation, therefore percentages are comparably small (considering that almost 70% of Finnish land is covered with forest)*

Forest Type	Pixel Value	Percentage over Finland
Deciduous Forest on Mineral Soil	18	3.18%
Deciduous Forest on Peat Land	19	1.18%
Coniferous Forest on Mineral Soil	20	19.08%
Coniferous Forest on Peat Land	21	3.73%
Coniferous Forest on Rocky Shore	22	0.83%
Mixed Forest on Mineral Soil	23	10.61%
Mixed Forest on Peat Land	24	5.09%
Mixed Forest on Rocky Shore	25	0.10%

The geometric accuracy of the CLC25m product is claimed to be high [42]. The average lengths of residual vectors are found to be around 11 meters which is less than half a pixel. Most vectors are less than 20 meters.

When compared to National Forest Inventory information, the overall classification accuracy of the CLC25m is around 90% at the first level wherein only five main classes are used: Artificial surfaces, agricultural areas, forests&semi-natural areas, wetlands and water bodies. At the second level, the forests were discriminated from the semi-natural areas and the overall accuracy was around 80%. At the third level, the forests were labeled within three main classes: Coniferous, deciduous and mixed forest and the accuracy was around 70% [42].

Production of CLC2006 was based on the same approach used in the production of CLC2000. The changes in the land cover have been detected using two methods combined: Evaluating differences between high-resolution land cover data sets of 2000 and 2006, and evaluating differences between satellite data only i.e. IMAGE2000 and IMAGE2006. Most of the changes in land cover were due to national forest management. Forest cuttings and forest re-growth activities made around 91% of all changes. Only 1% of all changes were caused by the enlargement of build-up areas. Clearing of new agricultural land covered 7%. Land cover changes from 2000 to 2006 affected only 2.1% of the whole Finnish territory [43].

In this thesis, CLC2006 25 x 25 meters resolution land cover map is used for the forest class dependent analysis. The original land cover map of the test site is given in Figure 3.2.

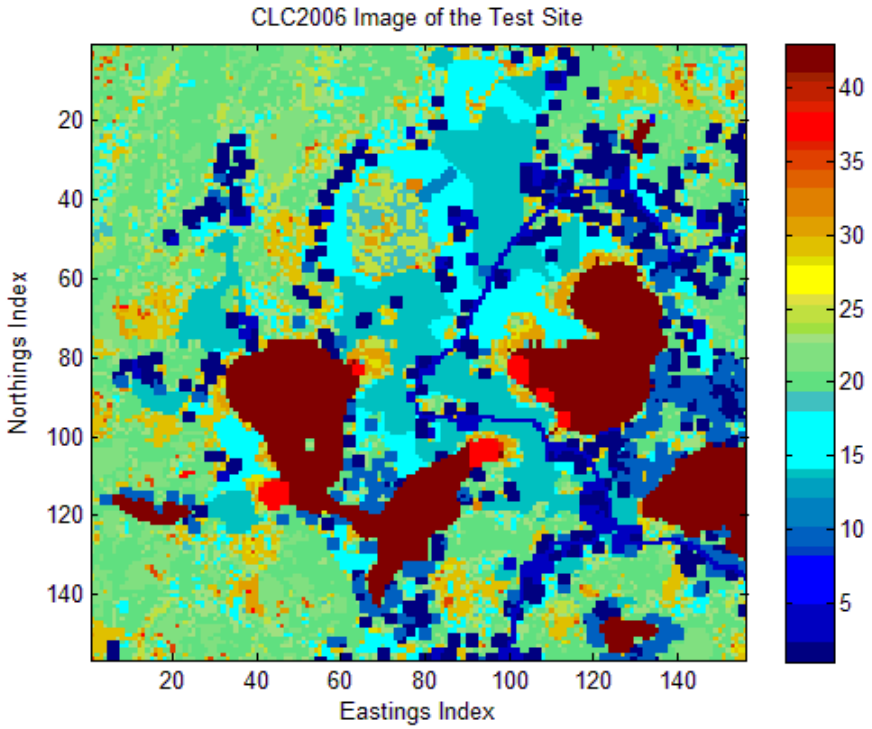

Figure 3.2 CLC2006 Land Classification Image of the test site in original form. *Every pixel corresponds to an area of 25 x 25 m. Image size is 3890 x 3890 meters. Tones of green (pixel intensities 18-25) correspond to the forested area of interest. Tones of yellow (pixel intensities 26-33) correspond to moor, meadows and sparse forest classes. Tones of dark blue (pixel intensities 1-3) correspond to urban and industrial areas. Regions of red (pixel value of 37) and dark red (pixel value of 43) represent the wetlands and lakes respectively. Tones of light blue (pixel values 14-15) correspond to the agricultural and open fields.*

3.3 Interferometric SAR Images

The radar data used in the thesis consist of 5 sets of dual-polarized (HH/VV) TanDEM-X/TerraSAR-X images acquired on dates September 4th, September 15th, October 18th, October 29th and November 9th of 2011.

TerraSAR-X (TSX) is Germany's first national remote sensing satellite that has been implemented in a public-private partnership between German Aerospace Center (DLR) and EADS Astrium GmbH. The objective of the mission is to provide high quality radar maps of the Earth's surface for a period of at least five years. The satellite has also been designed to satisfy the need of private sector for remote sensing data. It was successfully launched from the Russian spaceport Baikonur on June 15th, 2007 to its near-polar orbit around the Earth, at an altitude of 514 km. Its primary payload is an X-band radar sensor with a range of different modes of operation which allows it to record images with different swath widths, resolutions and polarizations. Since its day of release, TerraSAR-X has been acquiring many thousands data takes which have been further processed into image products. The quality of the products has been reported to often exceed the original requirements [44], [45].

TanDEM-X (TDX) stands for *TerraSAR-X add-on for Digital Elevation Measurements* and is a German satellite mission that has also been carried out as a public-private partnership between the DLR and EADS Astrium GmbH. It is a twin satellite of TerraSAR-X launched from the same station on June 2010, flying in a close formation only tens or a few hundred meters away, the two satellites have been imaging the same terrain simultaneously from two different angles. The main objective of the TanDEM-X mission is to produce a consistent Digital Elevation Model (DEM) of the Earth which is homogeneous in quality and unprecedented in accuracy from the bistatic X-Band SAR Interferometry. The TanDEM-X satellite has been designed for a nominal lifetime of five years and has a planned overlap of three years with TerraSAR-X. Together TanDEM-X and TerraSAR-X have provided the first single pass polarimetric interferometric data acquired from space which allows the acquisition of global-scale polarimetric interferometric data without the disturbing effect of temporal decorrelation [46], [47].

A TanDEM-X acquisition can be defined as a coordinated synthetic aperture radar (SAR) data take by both satellites TDX and TSX. During each TanDEM-X acquisition, both satellites are operated in instrument modes similar to those for the TerraSAR-X mission. Depending on their degree of cooperation, both satellites can act as one coordinated and synchronized SAR instrument, or just two separate ones. The TanDEM-X product characteristics such as focusing quality and radiometry are therefore determined by the effectiveness of this coordination. Acquisition geometry (effective baseline, incidence angle, along and across track separation etc.) also increases the complexity of the SAR system characteristics and leads TanDEM-X to be one SAR instrument with different sensitivities to different observables on the ground such as decorrelation, movements, height etc. [48].

The systematic processing of the TanDEM-X acquisition into the operational products was performed by DLR's Integrated TanDEM Processor (ITP) which has the functionalities of:

- Screening of TDX/TSX data takes at the receiving stations,
- Quality check of TDX/TSX joint acquisition,
- Bistatic SAR focusing to Co-registered Single Look Slant Range Complex Products (CoSSCs) as the intermediate products which are required for further interferometric SAR processing,
- InSAR processing with single and multi-baseline phase unwrapping,
- Production of raw DEMs as the input for the Mosaicking and Calibration Processor (MCP) [48].

The data delivered for this study included CoSSC products and also the final products of ITP processor e.g. lower resolution DEMs in geographical coordinates. However, in this master thesis, raw CoSSCs are interferometrically processed in order to achieve maximum resolution possible. Five sets of dual-pol (HH/VV) TanDEM-X dataset which were acquired in bistatic mode are used. The center frequency is 9.65 GHz for all acquisitions. The detailed information about the datasets can be found in Table 3.2.

Table 3.2 Properties of TanDEM-X/TerraSAR-X database used in this work

Acquisition Date	Acquisition Time	Effective Baseline [m]	Max. Inc. Angle [Deg.]	Min. Inc. Angle [Deg.]	Height of Ambiguity [m]	Orbit Direction
September 4, 2011	04:48:52-04:49:05	19.83	36.095	37.615	-301.77	Descending
September 15, 2011	04:48:52-04:49:06	20.24	36.090	37.618	-295.71	Descending
October 18, 2011	04:48:53-04:49:07	31.01	36.104	37.626	-190.66	Descending
October 29, 2011	04:48:53-04:49:06	30.81	36.100	37.617	-192.29	Descending
November 9, 2011	04:48:53-04:49:06	34.16	36.098	37.616	-173.23	Descending

Except the effective baseline which directly affects the height of ambiguity, parameters of acquisition geometry are very close to each other for all sets which provided a good opportunity for temporal variation analysis.

3.4 Tree Height Reference Measurements

In this study, tree height measurements obtained by a LIDAR (Light Detection and Ranging) instrument are used as the reference data. Also, the digital terrain model of the test site that is obtained by the same instrument is used in phase unwrapping step of interferometric chain followed by the thesis.

LIDAR is an optical remote sensing technology which measures the distance to the target by illuminating it by pulses (also known as Airborne Laser Scanning (ALS)). A typical LIDAR system consists of a LIDAR sensor, Inertial Navigation Unit (INU) and GPS. LIDAR sensor sends out the pulse of laser light and records both the travel time of the pulse and energy backscattered from the target. INU is used for correcting the pitch, roll and yaw of the aircraft. GPS is used for determining the accurate 3D position of the sensor relative to GPS base stations on the ground [49].

LIDAR is a cost effective way of generating high accuracy 3D digital terrain and surface models. It has been stated that LIDAR system can be effectively used for assessing vegetation characteristics due to its extensive area coverage, high sampling intensity, precise geo-locationing, accurate ranging measurements, and ability to penetrate beneath the top layer of canopy [50]. During last 10 years, LIDAR measurements have been extensively used in forestry directly or as auxiliary data. Many studies have been using the terrain elevation and canopy height models obtained by LIDAR for validation of the results obtained by other remote sensing techniques [10], [11], [38], [39].

LIDAR data used in this study was collected by laser scanner Optech ALTM 3100 unit with 100 kHz PRF. The year of acquisition was 2008 with flight altitude of approximately 1 km, and target point density of 3-4 pts/m^2. A digital surface (crown) model (DSM) relevant to treetops was obtained by taking the highest point within a 2 m grid. The missing points were interpolated by Delaunay triangulation [51]. The canopy height model (CHM) was obtained by simply subtracting the ground DEM from the corresponding treetop DSM. The crown DSM was calculated by means of the first pulse echo while the DEM used the last pulse echo. The accuracy of the obtained DEM was noted to be better than 20 cm for forested terrain. The CHM had a

-70 cm bias in the obtained tree heights and an RMSE of 0.5 m [11]. Figures 3.3 - 3.5 illustrate the ground model, canopy height model and the digital surface model of the test site:

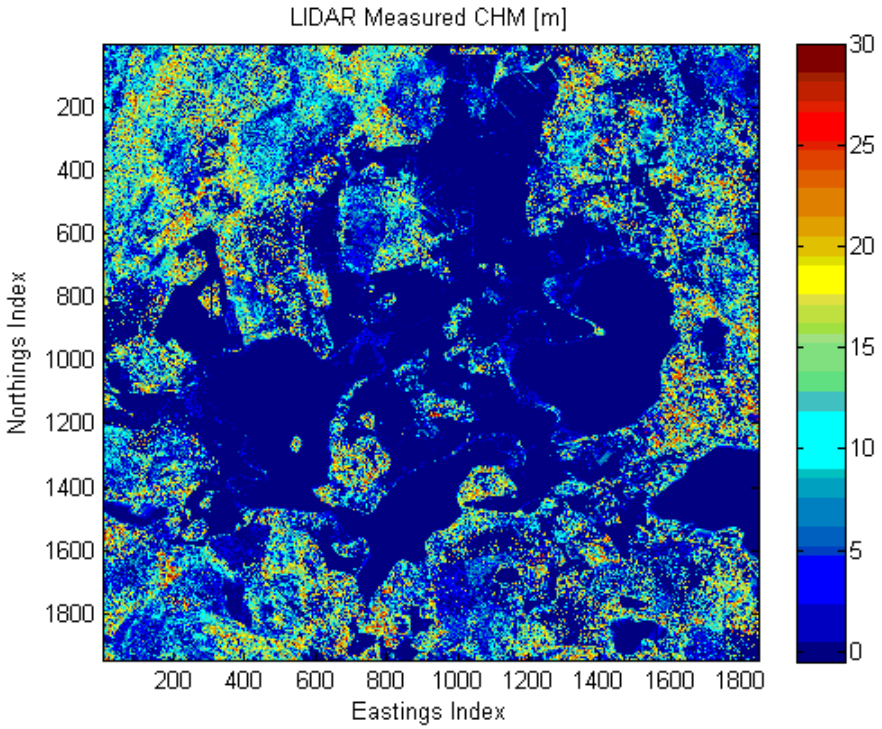

Figure 3.3 LIDAR measured canopy height model of the test site. *Size of the image is 3890 by 3890 meters.*

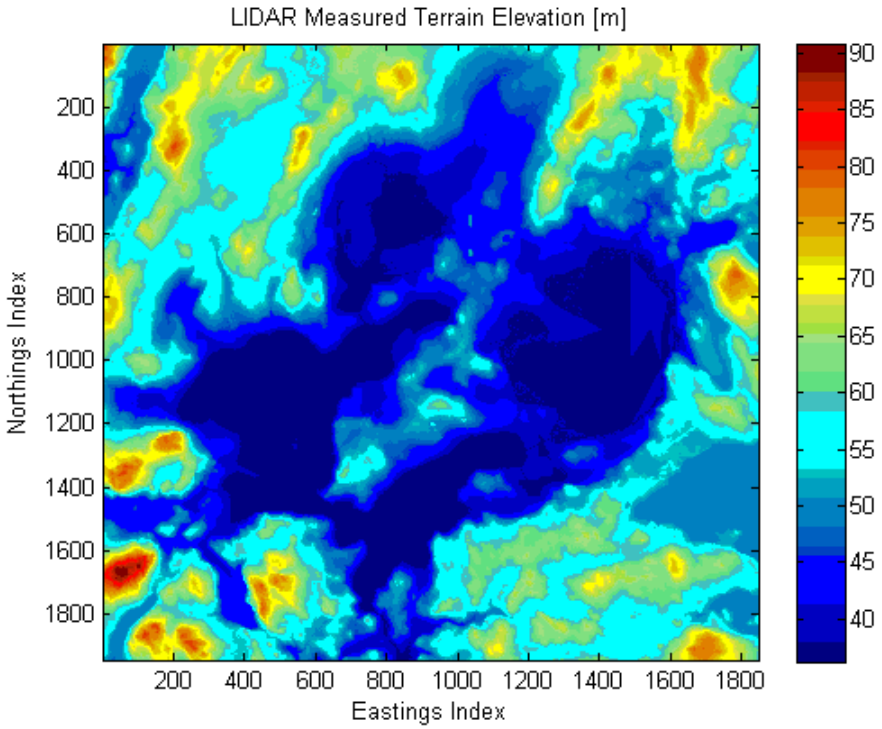

Figure 3.4 LIDAR measured digital terrain elevation model of the test site. *Size of the image is 3890 by 3890 meters.*

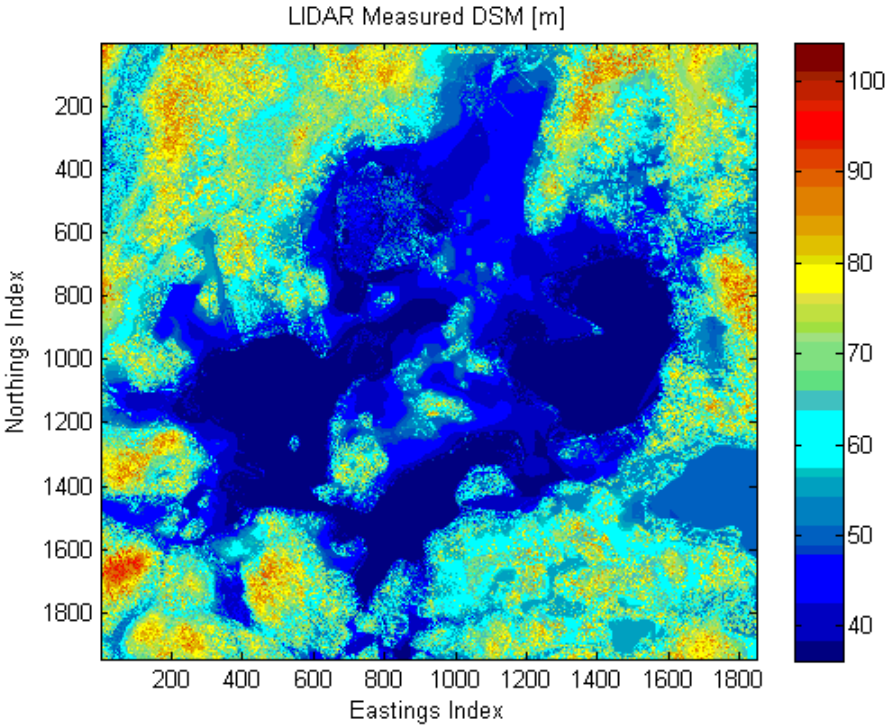

Figure 3.5 LIDAR measured digital surface (crown) model of the test site. *Size of the image is 3890 by 3890 meters.*

3.5 Weather Data

The weather history data used in this work is taken from Weather Underground (Wunderground) [52] for Kirkkonummi region of Finland. Wunderground is a commercial weather service which provides real-time weather information via the internet. It was founded as a part of the internet weather database of University of Michigan, in 1995. In the same year, Weather Underground, Inc. evolved as a separate commercial entity from the university. Since July 2, 2012, Weather Underground have been operating under the Weather Channel's subsidiary, the Weather Channel Companies, LLC. Weather Underground provides weather reports for most major cities across the world online and also local reports for newspapers and websites [53].

Wunderground history database contain hourly information of temperature, dew point, humidity, pressure, visibility, wind direction and speed, events and conditions such as rain, fog and average precipitation. The acquisition times of the TanDEM-X datasets differ only by seconds (see Table 3.2), around 04:48 - 04:49. Wunderground history data present weather information of every half an hour during the day. The time of the day that is closest to the TanDEM-X acquisition times is 04:50 on Wunderground database. Table 3.3 presents the weather conditions at 04:50 of the relevant dates. Temperature, humidity, wind speed and conditions are instant at 04:50 for the Malmi region of Helsinki which contains the test site. However precipitation information was not available for Malmi region, therefore data about the center Helsinki region is given for the previous three days before each acquisition.

Table 3.3 Weather conditions regarding the TanDEM-X/TerraSAR-X acquisitions. *Retrieved from [52].*

Acquisition Date	Temperature	Humidity	Wind Speed	Conditions	Precipitation of Previous Three Days
September 4, 2011	8.0 °C	100%	Calm	Mist	1.0 - 0.7 - 0.0 mm
September 15, 2011	13.0 °C	77%	16.7 km/h	Partly Cloudy	6.0 - 0.0 - 2.0 mm
October 18, 2011	9.0 °C	87%	20.4 km/h	Overcast	0.0 - 0.0 - 0.0 mm
October 29, 2011	10.0 °C	94%	14.8 km/h	Mostly Cloudy	0.0 - 0.0 - 0.0 mm
November 9, 2011	- 1.0 °C	100%	3.7 km/h	Fog	0.0 - 0.2 - 0.0 mm

Since SAR data that is used in thesis is obtained by bistatic single-pass TanDEM-X acquisitions, temporal decorrelation is not effective. Therefore wind speed is not a factor of interest anymore. However other factors affect the reflectivity of the forest, therefore also the parameters investigated in this thesis.

4. Processing of the Data

The TanDEM-X and TerraSAR-X data delivered includes 8 sets of Coregistered Single look Slant Range Complex (CoSSC). CoSSCs are the intermediate products produced by DLR's Integrated TanDEM Processor. Since they are already co-registered complex images, they are to be interferometrically processed by the user for generation of DEM's or further purposes such as coherence behavior analysis, production of land classification maps etc.

Only 5 sets of CoSSCs had very similar acquisition geometry, time and coverage of the Finland and therefore used in this work (see Section 3.3). Data processing in this work have been done in two main steps: Pre-processing and post-processing. Section 4.1 presents the steps and algorithms used in pre-processing and Section 4.2 gives a detailed overview of post-processing.

4.1 Pre-processing

Pre-processing of the CoSSCs includes the steps of conversion of CoSSC products into 32-bit complex floating point format for MATLAB processing, interferometric coherence calculation by the converted complex images, vertical wavenumber calculation, flat earth phase removal and geocoding. Final outputs of the pre-processing are complex coherence and vertical wavenumber maps of the 5 sets of TanDEM-X dual-polarimetric (HH/VV) in WGS84 Geographic Coordinate System.

4.1.1 Conversion of CoSSC Products

The CoSSC files originally come with the extension of ".cos". DLR has released TerraSAR-X/TanDEM-X SSC/CoSSC Reader for IDL and ENVI on February 01, 2012. However, there is no officially released SSC/CoSSC reader for MATLAB yet.

In order to read the data in MATLAB, CoSSCs are converted into 32-bit complex floating point format with a Java software which was made available in an earlier project [54]. The dimensions of the converted CoSSC products are presented in Table 4.1.

Table 4.1: Dimensions of the converted CoSSC products with respect to acquisition date

Acquisition Date	Dimensions
September 4, 2011	12346 x 24098
September 15, 2011	12334 x 24098
October 18, 2011	12368 x 24098
October 29, 2011	12368 x 21526
November 9, 2011	12368 x 24098

4.1.2 Reading Converted Products in MATLAB

Since the format of the data is 32-bit complex floating point, it is not possible to read whole data using MATLAB on 4 GB Random Access Memory (RAM) computers. Thus, the data is preferred to be read in smaller regions that include the test site. As an example, absolute value maps of the master and slave complex images are given in Figure 4.1 and Figure 4.2. The date of acquisition is September 4, 2011 and the polarization mode is HH. Images are in slant range coordinates. Topography-related information is visible on both slave and master images. Since the backscattering from lakes is lower than the rest, they look darker. Also angle of the same complex images are given in Figure 4.3 and Figure 4.4. Figures suggest that the phase of a single SAR image is just a random noise. Subsection 4.1.3 will show how two random noises can produce a useful phase pattern with interferometric coherence calculation.

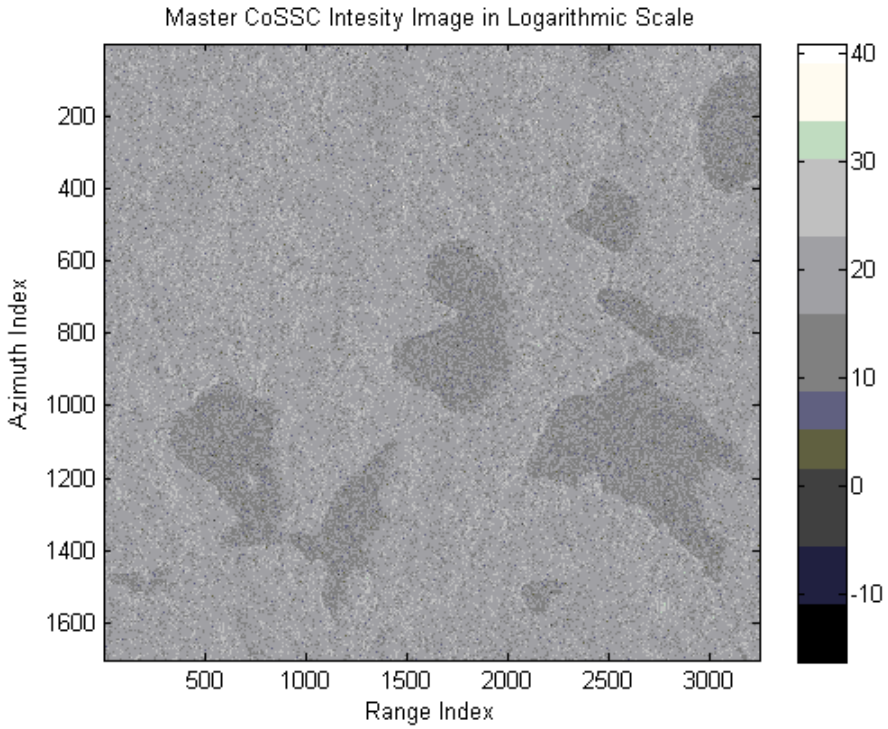

Figure 4.1 Absolute value of the complex TerraSAR-X image (Master). *The date of acquisition is September 4, 2011 and unit of the colorbar is decibels.*

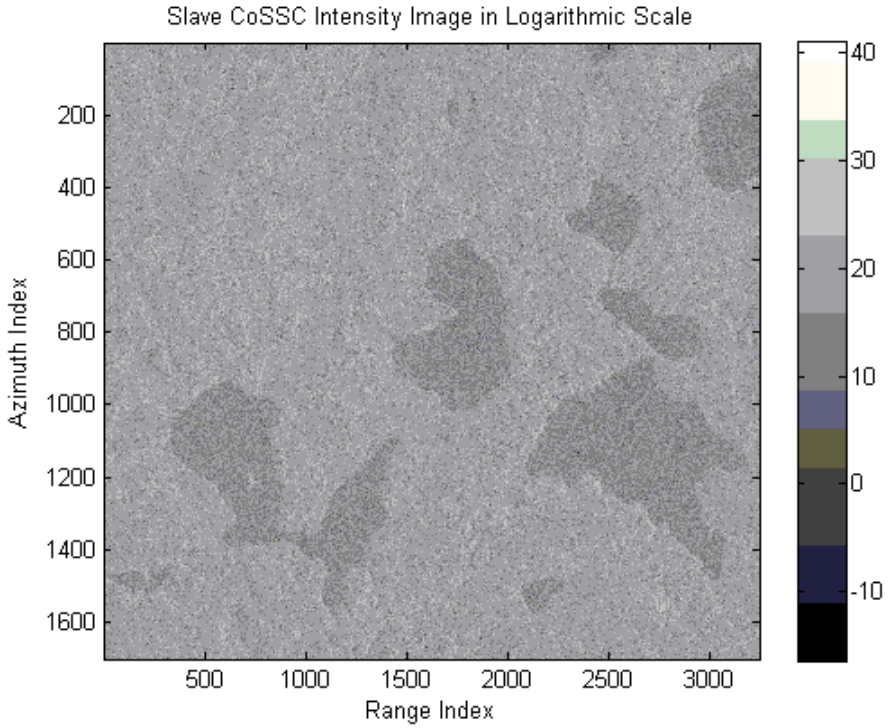

Figure 4.2 Absolute value of the complex TanDEM-X image (Slave). *The date of acquisition is September 4, 2011 and unit of the colorbar is decibels.*

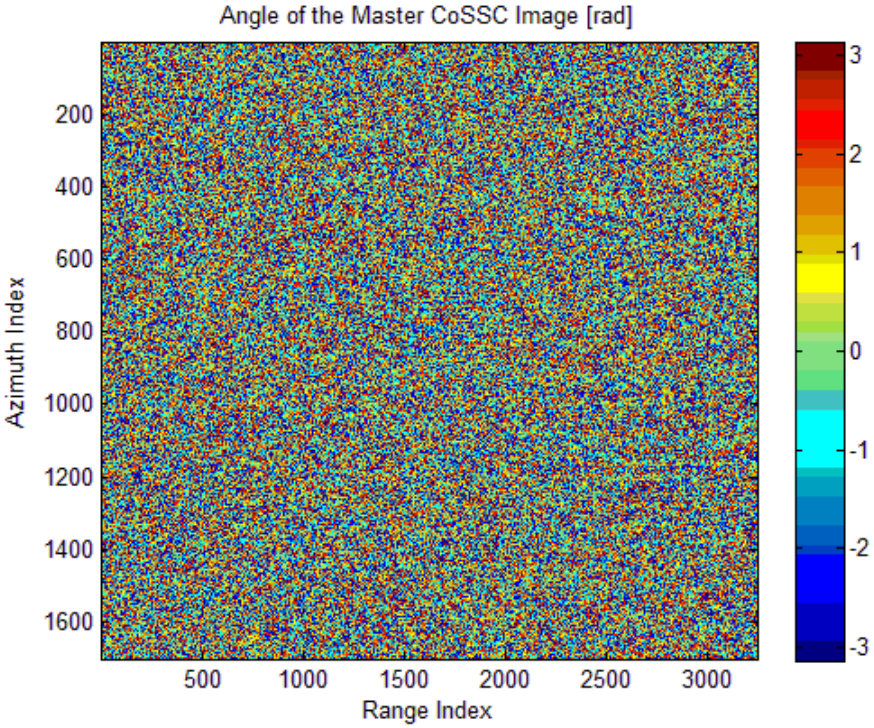

Figure 4.3 Phase of the complex HH-pol TerraSAR-X image (Master). *The date of acquisition is September 4, 2011.*

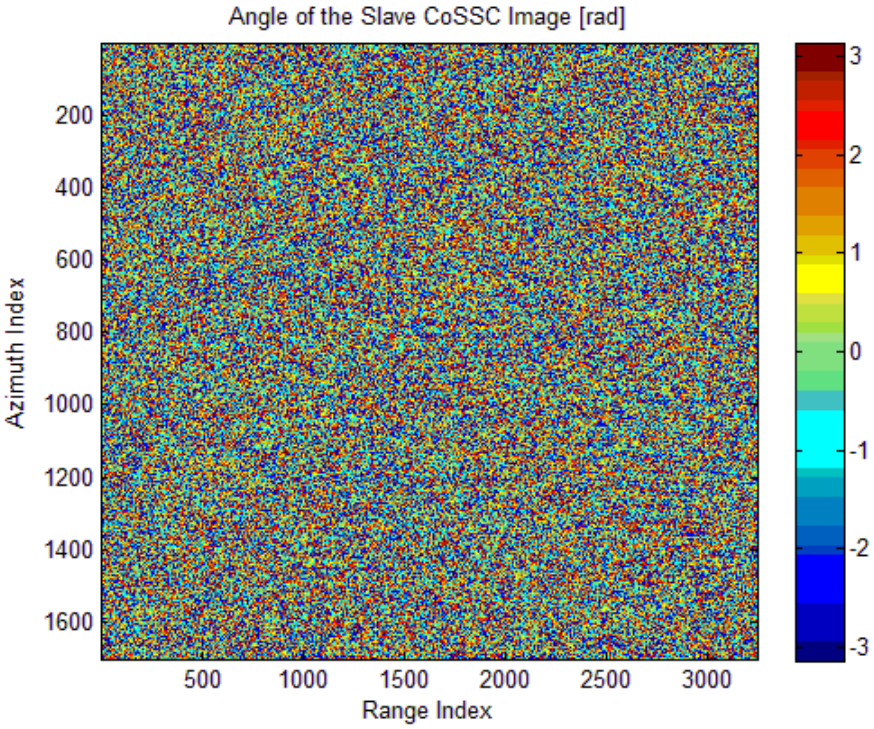

Figure 4.4 Phase of the complex HH-pol TanDEM-X image (Slave). *The date of acquisition is September 4, 2011.*

4.1.3 Interferometric Coherence Calculation

As already shown in Equation 3.8, coherence of the complex images is estimated through a maximum likelihood estimator in the form:

$$C = \frac{\sum_{k=1}^{n} I_1(\mathrm{k}) * \mathrm{conj}(I_2(\mathrm{k}))}{\sqrt{\sum_{k=1}^{n} I_1(\mathrm{k}) * \mathrm{conj}(I_1(\mathrm{k}))}\sqrt{\sum_{k=1}^{n} I_2(\mathrm{k}) * \mathrm{conj}(I_2(\mathrm{k}))}} \tag{4.1}$$

I_1 and I_2 refer to the master and slave complex images respectively; n is the number of pixels in the estimation window. For this work, estimation window was chosen to have dimensions of 15 x 15, whereas each pixel of the window has equal weight. Figure 4.5 shows the absolute value of the coherence for the HH-pol set acquired on September 4, 2011 obtained by Equation 4.1. Figure 4.6 presents the phase of the coherence for the same set. Since geocoding has not been done yet, the maps are in slant range coordinates.

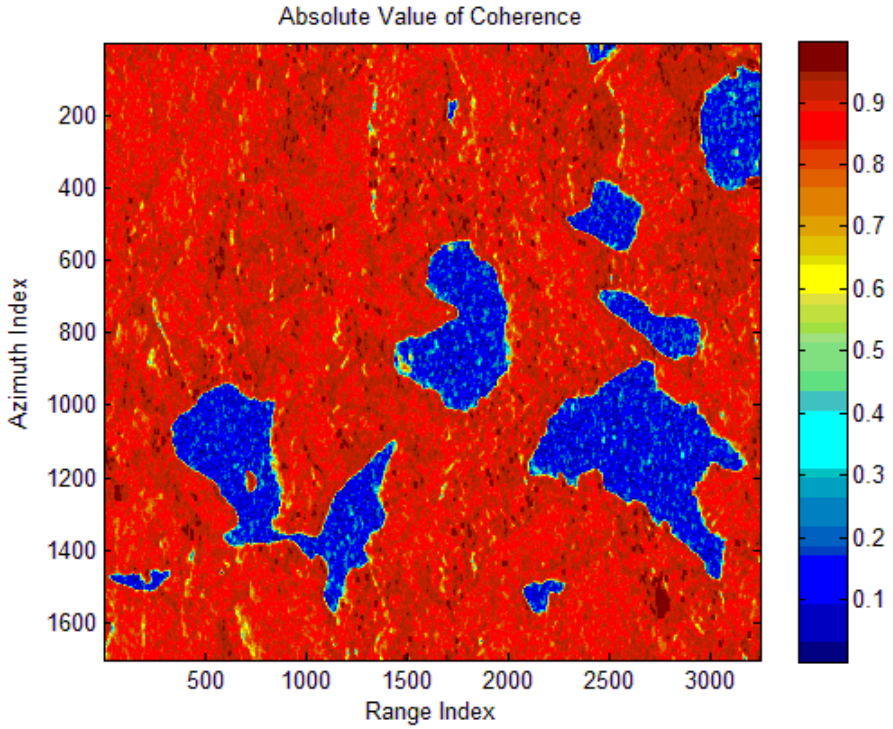

Figure 4.5 Absolute value of the complex coherence for the set acquired on September 4, 2011. *Calculated with an estimation window of 15x15. Tones of blue correspond to lakes in the region (see the colorbar).*

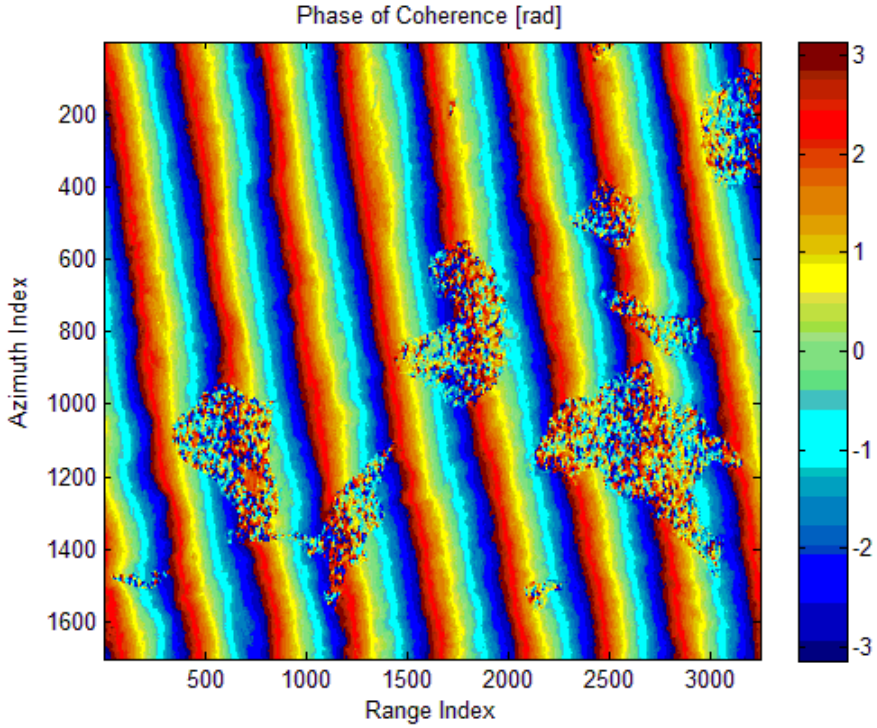

Figure 4.6 Phase of the complex coherence for the set acquired on September 4, 2011. *Calculated with an estimation window of 15x15. The colorbar is in radians. Fringes seem to have a constant frequency. A tilt is observed due to the displacement in azimuth direction.*

4.1.4 Vertical Wavenumber Calculation

The vertical wavenumber k_z is a parameter that includes interferometric information specific to measurement setup. It is directly related to the radar frequency f, incidence angle θ_i and incidence angle difference between each interferometric measurement $\Delta\theta_i$. k_z is calculated as:

$$k_z = \frac{4\,\pi\,(\Delta\theta_i) f}{c(\theta_i)} \tag{4.2}$$

Above, c represents the speed of the light. Vertical wavenumber varies along the range and depends on the flight track [11]. Vertical wavenumber maps are later going to be used in phase unwrapping. Figure 4.8 presents the vertical wavenumber map for the data acquired on September 4, 2011. The incidence angles are calculated by the header files that contain information about the acquisition geometry of the

coregistered products. Polarization mode is HH and the map is in slant range coordinates.

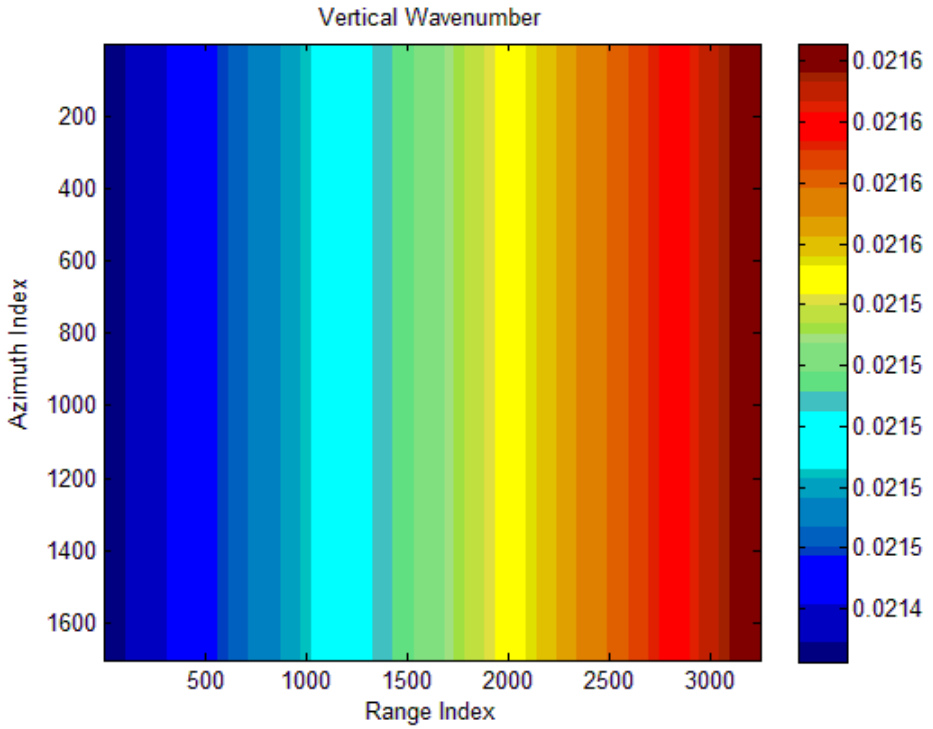

Figure 4.7 Vertical wavenumber for the acquisition on September 4, 2011. *In azimuth direction, the value is constant, however in the range direction it increases.*

.

4.1.5 Flat Earth Phase Removal

In Subsection 2.3.4, the decomposition of the interferometric phase into several parameters was demonstrated. The first term of the decomposed interferometric phase (see Equation 3.12) is always present in SAR measurements since the slant range displacement grows bigger with the increasing incidence angle. Therefore, the flat earth pattern has to be removed in order to obtain pure elevation above the measured area. The flat earth phase map is produced using the equation provided by [55]

$$fe = exp\left(\frac{-4\,\pi\,j\,(B_{eff})\,\Delta R}{\lambda\,(R_i)\tan(\theta_i)}\right) \tag{4.3}$$

whereas ΔR corresponds to the slant range displacement in terms of incidence angle. For the same set of TanDEM-X/TerraSAR-X data which is used in the previous

subsections, phase of the flat earth removal matrix looks like as in Figure 4.9 disregarding the tilt in azimuth direction:

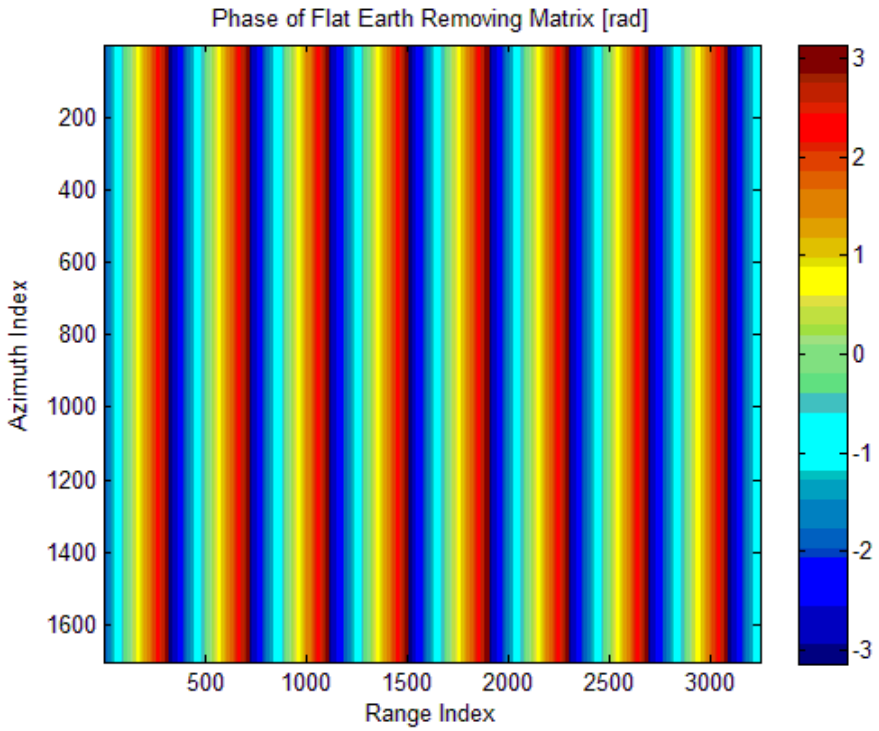

Figure 4.8 Phase of the flat earth removal map. *Acquisition date of the data is September 4, 2011 and the polarization mode is HH. Effect of the displacement in azimuth direction is not taken into account.*

After multiplication of the flat earth removing matrix with complex coherence map shown in Figure 4.7, the result showed that the flat earth phase removal was not successful. Figure 4.10 shows the outcome of the unsuccessful operation. Here, in range direction, phase seems to be successfully removed; however in azimuth direction it is obvious that the operation was unsuccessful. Thus, it has been compulsory to consider the effect of displacement in the azimuth direction. Since the displacement information was not available in the header files of the dataset, it is calculated from the original interferometric phase maps and optimized by inspection for each dataset. The outcome of the tilting process, the new flat earth phase removing matrix, is shown in Figure 4.11. The final products of the flat earth phase removal are calculated by matrix multiplication of the new flat earth removing matrices with the

complex coherence maps. Figure 4.12 shows the final version of the coherence angle map. The correction made removes the phase pattern also in azimuth direction. Topographic information can easily be seen and the maps are ready for the next steps of interferometric processing chain.

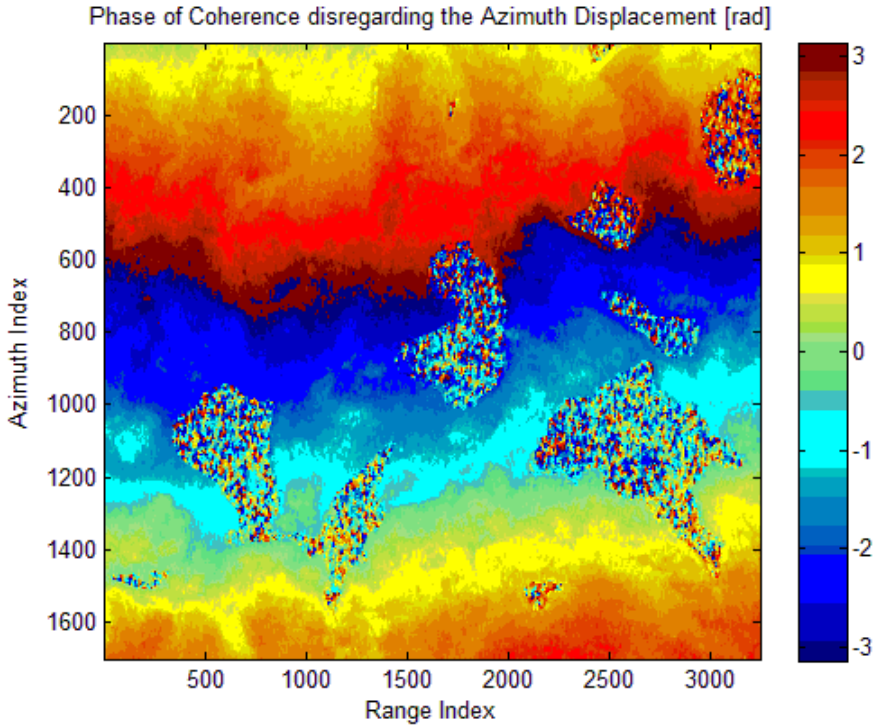

Figure 4.9 Phase of the complex coherence after unsuccessful flat earth removal.

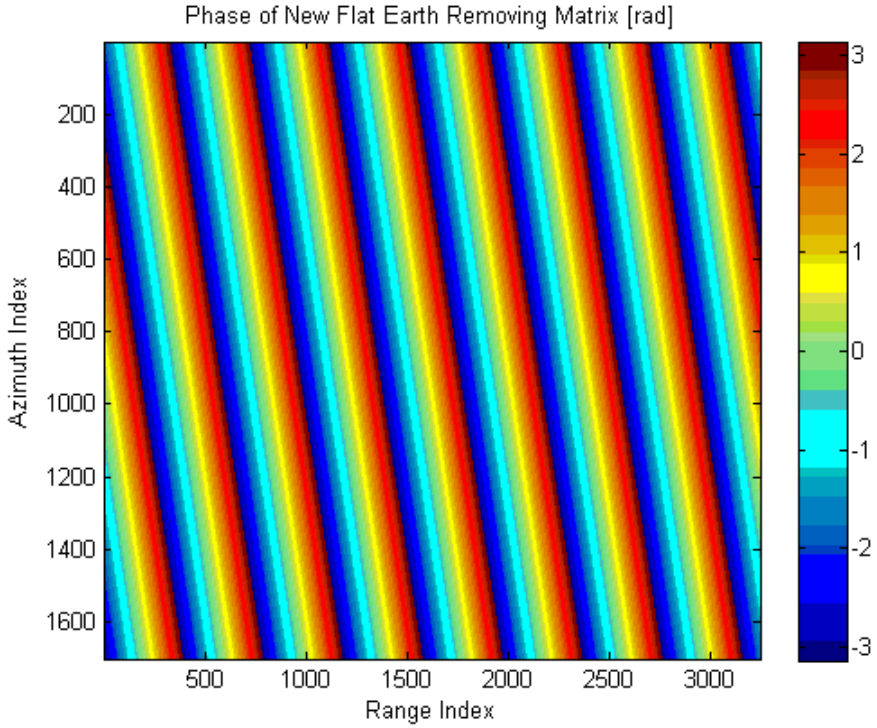

Figure 4.10 Phase of the new flat earth removal map considering the effect of azimuth displacement.

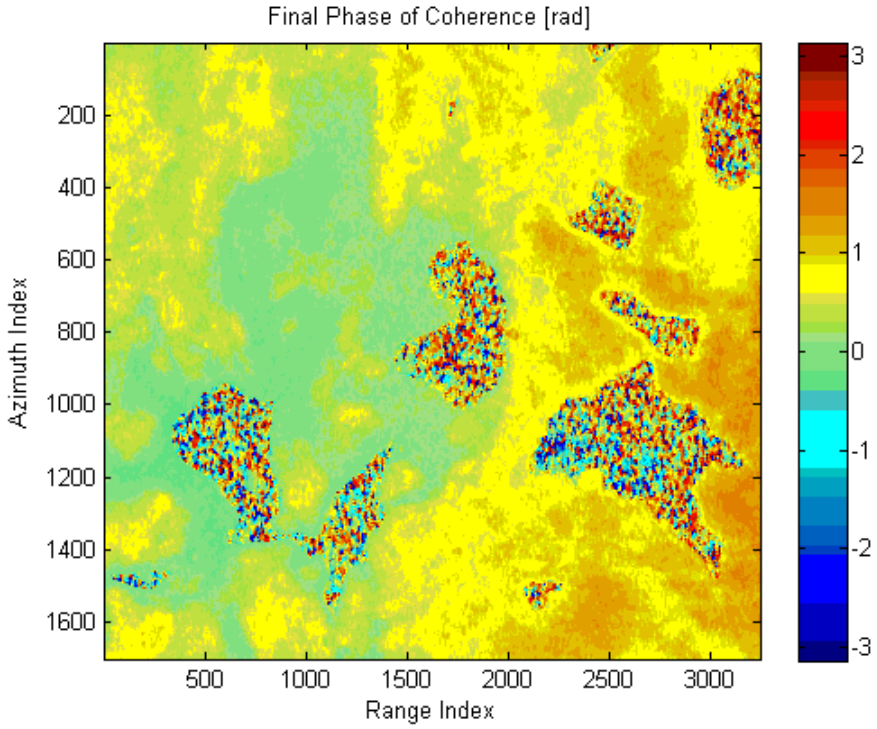

Figure 4.11 Phase of the complex coherence after successful flat earth removal.

Phase pattern in azimuth direction is also removed after the correction made.

4.1.6 Coordinate System Transformation

After the completion of flat earth phase removal stage, coherence and vertical wavenumber maps are needed to be transformed into a common coordinate system with the ground truth maps, namely, LIDAR CHM, DTM and CLC2006 land cover maps. LIDAR CHM and DTM were received in UTM coordinates, CLC2006 was in Finnish National Grid Coordinate System and the processed TanDEM-X/TerraSAR-X data are in slant range coordinates. As the common coordinate system, UTM was chosen since it is well-known and commonly used. The corner coordinates of the LIDAR data was known beforehand and thus area covered by LIDAR is chosen as the test site (see Section 3.1). It is preferred first to transform the corner coordinates from UTM coordinates to Finnish National coordinates, and then basically the corresponding region is cropped from the CLC2006 land classification map. Transferring the TanDEM-X/TerraSAR-X data to UTM coordinates has been done using the algorithm developed during the project [54]. One can check [54], [56] for more information about process. Errors in the order of a few meters are corrected by comparing the coherence maps with LIDAR and CLC2006 maps. Offset values are set to the algorithm until the perfect fit between all maps are achieved. A sample result of the coordinate transformation is given in Figure 4.13. Phase of the complex coherence for the data obtained on September 4, 2011 is shown. Small amount of holes observed in the map are due to the nature of the transformation process and also blue regions observed around some of the corners. They are represented as NaNs (not-a-number) in the image where the information about them does not exist. The resolution of the image is 2 x 2 meters and the dimensions are 1945 x 1945, therefore representing a total area of 3890 x 3890 meters.

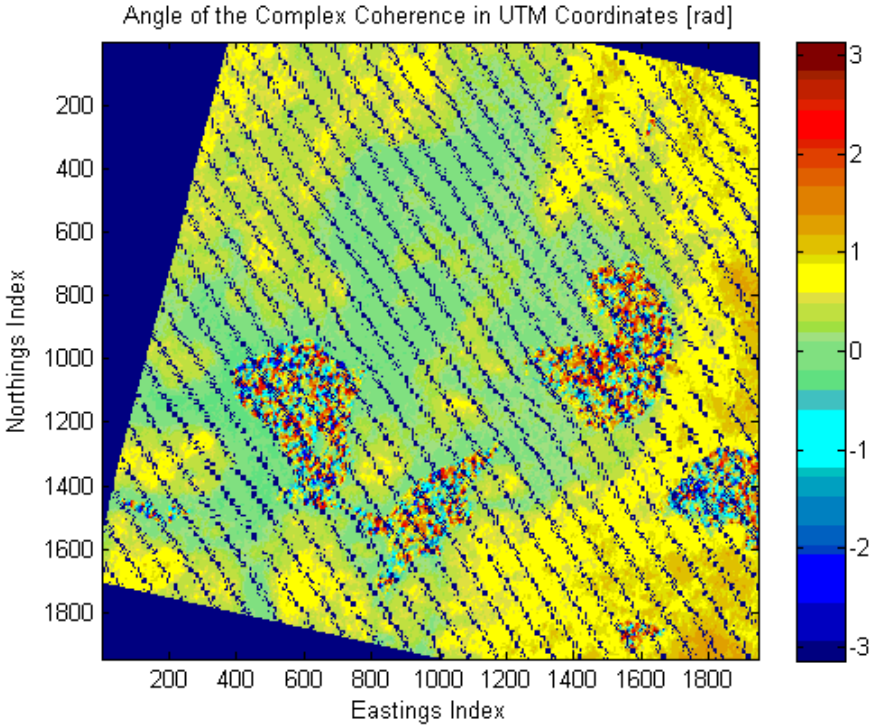

Figure 4.12 Phase of the complex coherence after the conversion to UTM coordinates.

Two-dimensional linear interpolation is applied in order to recover the missing pixels in the coherence and vertical wavenumber maps. Results of the interpolation are shown in Figures 4.14 and 4.15.

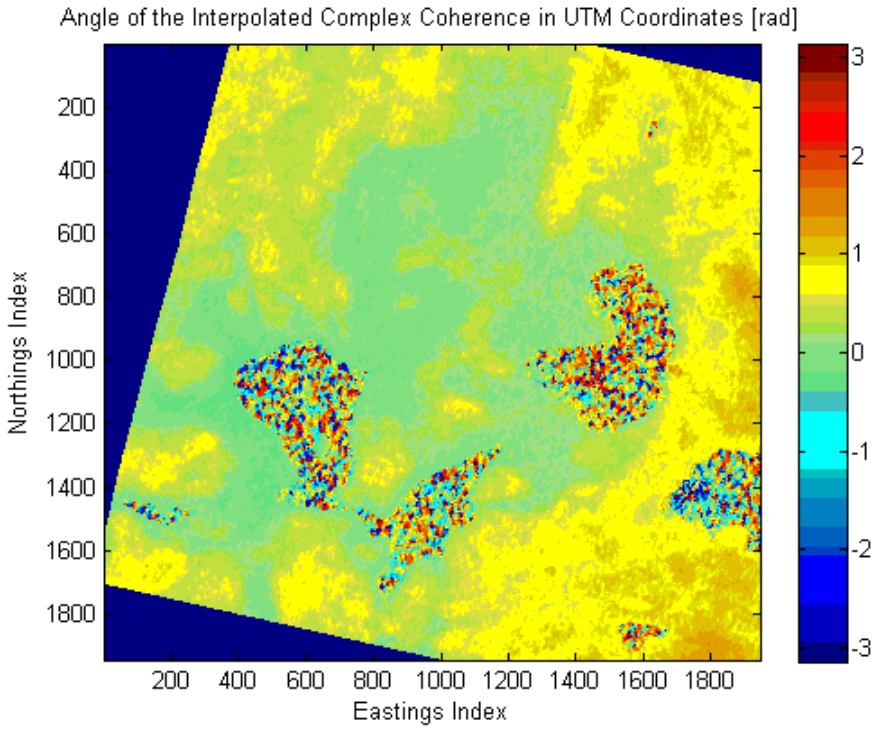

Figure 4.13 Phase of the complex coherence after two-dimensional interpolation in UTM coordinates.

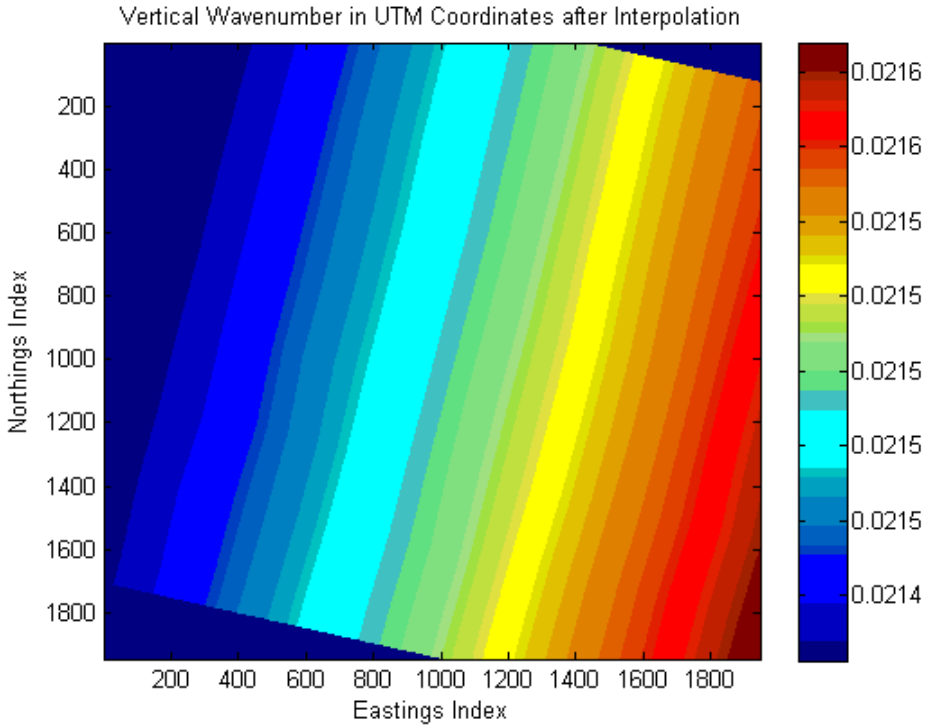

Figure 4.14 Vertical wavenumber after two-dimensional interpolation in UTM coordinates.

4.2 Post-processing

In this section, the steps of the post-processing are described. Subsection 4.2.1 presents the method applied for fitting the LIDAR ground phase to the interferometric SAR phase and the results of the fitting operation. Subsection 4.2.2 describes how the tree heights are retrieved from the interferometric SAR phase. Finally, Subsections 4.2.3 and 4.2.4 present the last steps of the whole processing chain. Specifically, the method followed in retrieval of interferometric coherence statistics is described in Subsection 4.2.3, and Subsection 4.2.4 presents the method used in calculation of SPC height, penetration depth and relative location of SPC to treetop statistics.

4.2.1 Phase Unwrapping

Phase unwrapping is one of the key steps of interferometric chain for generation of DEM's. It is applied by adding the correct integer multiple of 2π to the interferometric fringes. There are several methods of phase unwrapping, in this work it is preferred to fit the LIDAR measured ground phase to the interferometric SAR phase as proposed in [10] and [11]. LIDAR Digital Terrain Model (DTM) and Canopy Height Model (CHM) are highly accurate measurements of forest vertical structure and Digital Surface Model (DSM) is simply obtained by their addition. For SAR measurements, highest coherence values usually belong to the open areas; consequently those areas are the most accurately measured regions. Therefore, it is preferred to fit the LIDAR measured DSM phase to the SAR phase through open areas. Equations 4.4 and 4.5 introduced in [11] describe how the fitting is done. Using the vertical wavenumber k_z, the original LIDAR DTM h_{dtm} and two unknowns h_{int} and φ_{int} later to be retrieved by the optimization problem (4.5), the wrapped phase φ_w of the LIDAR DTM is obtained.

$$\varphi_w = k_z (h_{dtm} + h_{int}) + \varphi_{int} \tag{4.4}$$

$$\{h_{int}, \varphi_{int}\} = \arg\min \Sigma \left|\left|\exp\left(j(k_z (h_{dtm} + h_{int}) + \varphi_{int})\right) - \exp\left(j\varphi_{ground}\right)\right|\right|^2 \tag{4.5}$$

where φ_{ground} is the measured ground phase of the open areas. Open areas are determined using the absolute value of all five sets of coherence maps. The product $|C|_{ground}$ of coherences is calculated as:

$$|C|_{ground} = |C|_1|C|_2|C|_3|C|_4|C|_5 \quad (4.6)$$

where C_i's are the complex coherences of five TanDEM-X pairs. The pixels satisfying the condition $|C|_{ground}$ > 0.4 and having the average tree height less than 3 meters (calculated within a 10 x 10 averaging window) are used in the optimization problem since the interferometric coherence should be high and canopy height should be really low for open areas. The points satisfying the aforementioned conditions are validated using land cover data. Solutions h_{int} , φ_{int} of the optimization problem are used in Equation 4.4 and finally, LIDAR DTM phase is fitted to the each interferogram separately. Figure 4.15 shows the result of the fitting operation using the SAR data obtained on September 4, 2011. Comparing SAR phase (Figure 4.13) with LIDAR DSM phase, it is not easy to claim that the fitting operation was successful. For better comparisons, two strips of LIDAR DSM phase and SAR phase are plotted in north-south and east-west directions. Strips correspond to the 1000th column and 1000th row of the maps. Figure 4.16 shows the phase profiles in east-west and Figure 4.17 shows the phase profiles in north-south direction.

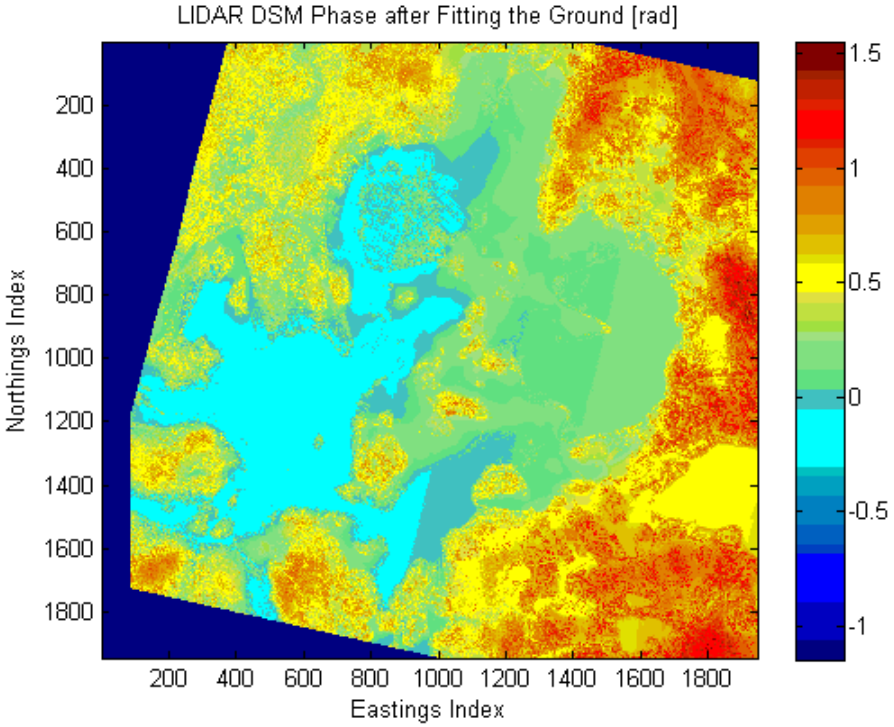

Figure 4.15 LIDAR measured DSM phase angle after the fitting operation.

Resolution is 2 x 2 meters. Dark blue regions around some of the corners contain no information and represented by not-a-number (NaN) in MATLAB.

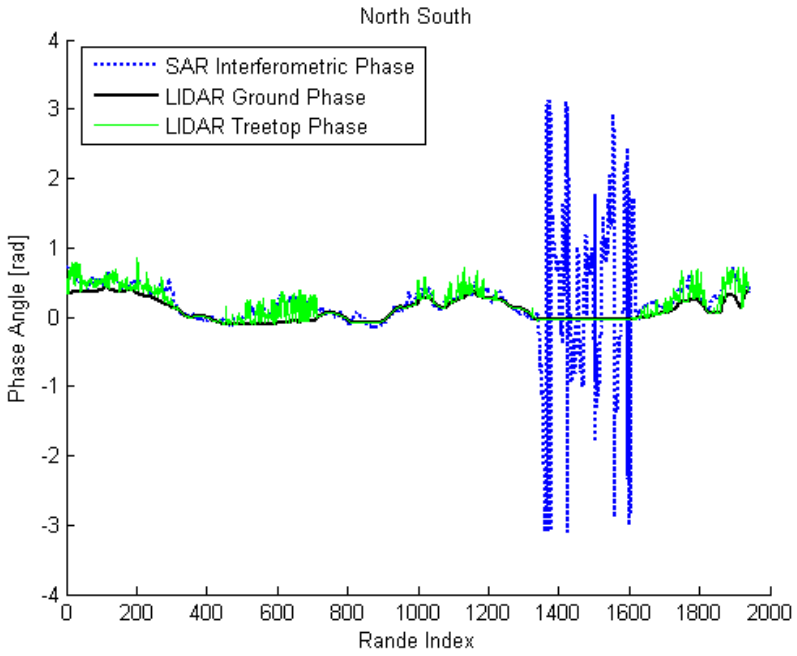

Figure 4.16 SAR, LIDAR ground and treetop phase heights in vertical direction. *Profiles correspond to the 1000th column of the SAR phase angle, LIDAR DTM and LIDAR DEM maps.*

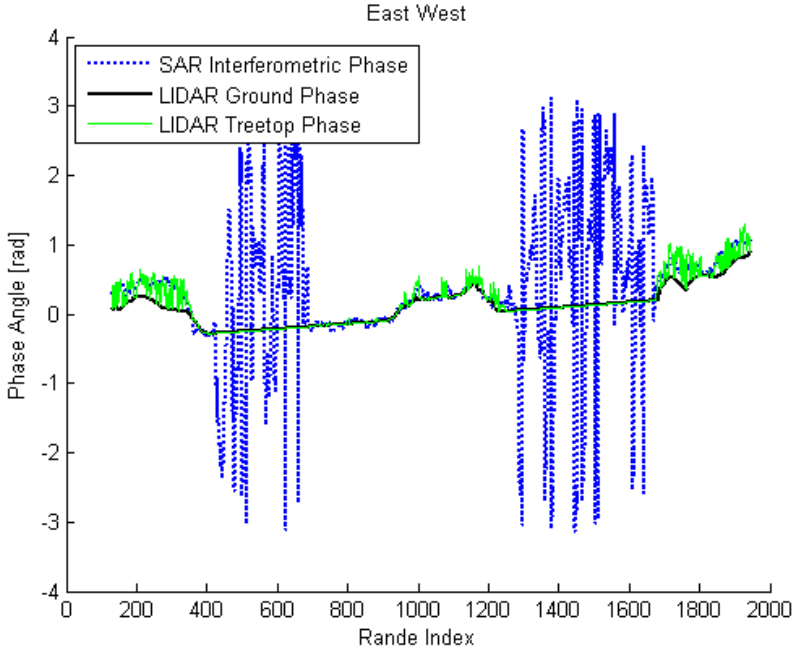

Figure 4.17 SAR, LIDAR ground and treetop phase heights in horizontal direction. *Profiles correspond to the 1000th row of the SAR phase angle, LIDAR DTM and LIDAR DSM maps.*

According to Figures 4.16 and 4.17, the LIDAR ground phase and SAR interferometric phase are in good agreement. The big oscillations in the SAR interferometric phase are caused by the lakes where SNR is very poor. In comparison to variations in LIDAR treetop phase, oscillations caused by the water are much higher since the height of ambiguity for the TanDEM-X/TerraSAR-X acquisition at September 4, 2011 is -301.77 meters which is almost ten times higher than the maximum tree heights (~30 m) in the test site. For other four sets of TanDEM-X/TerraSAR-X acquisitions, the same procedure is applied and for each set, LIDAR ground phase is wrapped to SAR phase one by one.

4.2.2 Retrieval of Tree Heights by SAR Coherence Phase

In order to investigate temporal variations in scattering phase center (SPC) height and related parameters with respect to forest type, the tree height map from the SAR phase needs to be extracted. First, ground phase in SAR coherence phase is removed by simply multiplying it with the complex conjugate of fitted LIDAR ground phase. After removal, absolute value of the SAR phase is directly related to the tree heights by vertical wavenumber:

$$|\varphi_{int}| = (k_z)(h_{int}) \tag{4.7}$$

Figure 4.18 illustrates the CHM retrieved directly by SAR interferometric phase of the set acquired on September 4, 2011. Because of the noisy nature of the TanDEM-X/TerraSAR-X data, there are some regions with retrieved tree heights larger than 30 meters. That is not possible according to the forest inventory information and highly accurate LIDAR CHM measurements of 2008. However, between 2008 and 2011, a little more growth can be expected in forest heights, therefore tree heights larger than 32 m are equalized to 32 m instead of 30 m.

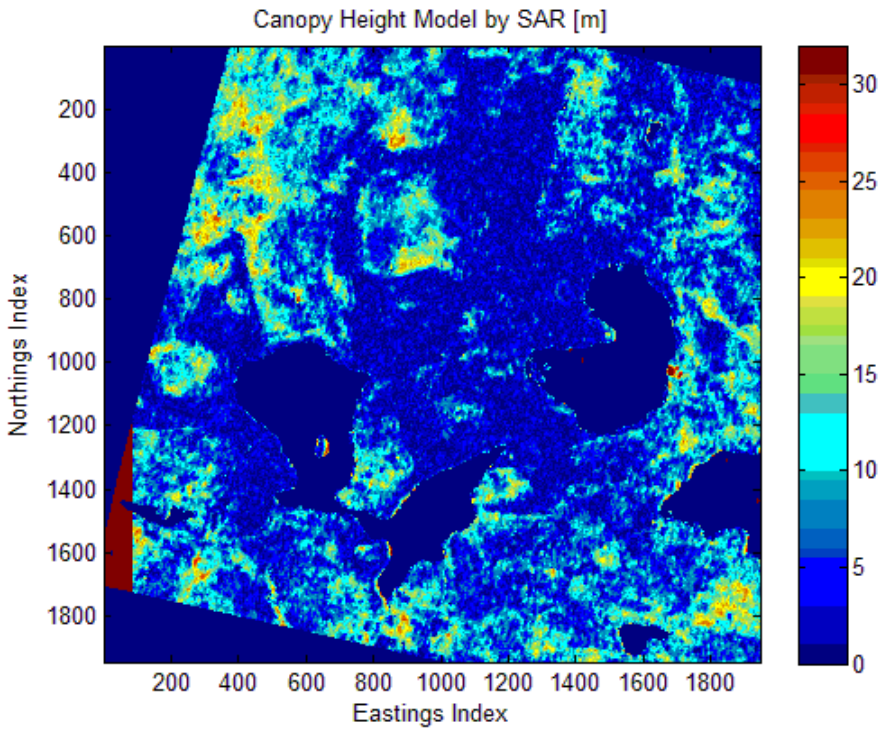

Fig 4.18 TanDEM-X/TerraSAR-X canopy height model retrieved by the data acquired on September 4, 2011. *Red region around the eastings index [0, 88] and northings index [1200, 1700] will be filtered afterwards.*

4.2.3 Retrieval of SAR Coherence Statistics

For each of interferometric pair acquired on September 4, 2011, September 15, 2011, October 18, 2011, October 29, 2011 and November 9, 2011; interferometric SAR coherence maps were obtained for both the HH and VV polarized datasets. Since none of the maps had the same coverage of test site, only the common region that exists on each map is taken into account. The original CLC2006 land classification map was in 25 x 25 meters resolution. Upsampling with nearest neighbor interpolation is therefore applied to the CLC2006 image in order to satisfy pixel by pixel matching between SAR and CLC2006 images. Finally for the dominant forest classes in CLC2006 image, mean and standard deviation of the coherence amplitudes are calculated pixelwise.

4.2.4 Retrieval of SAR SPC Height and Related Statistics

As already mentioned in Subsections 2.2.2 and 2.2.3, volume scattering is the dominant scattering mechanism in vegetation and therefore the scattering center is expected to be somewhere between upper surface of the vegetation and the ground. SPC height is an indicator of the penetration depth of the SAR signal into the vegetation canopy. Dense forest is expected to have lower penetration depths in comparison to sparse forest, therefore higher SPC heights. Also, leaf-on and leaf-off conditions are expected to affect SPC heights and the penetration depths. It is expected that in the leaf-on conditions of the summer and early fall the SPC heights should be located to be nearer to the upper surface of the canopy compared to leaf-off conditions of winter time for deciduous forest. Also, an increase in penetration depth is expected while leaves/ needles of the trees change their color which results in lower reflectivity due to decreasing water content.

In order to examine the variations in SPC heights and penetration depths with respect to forest type during the season of fall, three variables are analyzed. The first variable is the mean of SPC heights with respect to forest class. It is preferred to define it as the average of CHM maps which is basically the average tree height when it is directly derived by interferometric phase. Pixel by pixel for the corresponding forest class, the average retrieved tree height is calculated separately for each CHM.

The second parameter investigated is the penetration depth of the SAR signal. It is preferred to characterize it as the difference of LIDAR measured CHM and the CHM retrieved by SAR coherence phase. In this analysis, the height difference is calculated for each pixel with LIDAR CHM heights higher than 10 meters since it has been claimed that a ground contribution to the SAR return signal is highly probable for tree heights less than 10 m [11]. The negative values caused by SAR tree heights that exceed LIDAR's are also taken into account. Pixel by pixel for each forest class of interest, the average penetration depth is calculated, again individually for each dataset.

The third parameter, relative location of SPC to the treetop is calculated by dividing the SPC height to the LIDAR tree height for each pixel for tree heights higher than 10 meters in LIDAR CHM. The parameter defines the relevant location of SPC with

respect to the LIDAR tree height. Again, it is calculated for each forest class of interest, specific to each dataset.

Those parameters do not present the precise values due to the facts that:

- LIDAR data was obtained in 2008 and TanDEM-X/TerraSAR-X dataset were acquired in 2011. In the three years between those acquisitions, forest is expected to grow and also there might be some harvesting.

- Due to highly noisy nature of TanDEM-X/TerraSAR-X dataset, coherence calculation is done in an 15 x 15 equally weighted averaging window, thus SAR coherence phase is not highly sensitive to the fast variations in forest canopy structure whereas LIDAR is.

- Original resolution of LIDAR data was also diminished to 2 x 2 meters which also has deteriorated the forest information.

- Due to the coordinate transformation from slant range to UTM, there have been some pixels with no information produced. They were filled by linear two-dimensional interpolation; however this process deteriorates the forest sensitive information in SAR images.

Despite the fact that those parameters do not provide precise information about SPC and other statistics, they can be used to map the temporal variations in forest satisfactorily. Since the focus of this study is to analyze the temporal and forest class-specific variations in average forest parameters, neither big coherence averaging window nor 3 year difference between the LIDAR and SAR acquisitions constitute a problem for the relativity analysis that has been conducted. However, accuracy of the relativity analysis is reduced considerably due to resolution and classification accuracy of the CLC2006 land cover database. The original resolution of the database was 25 x 25 meters, which is actually very low in comparison to radar data with 2 x 2 meters resolution. Also, it has been reported that classification accuracy of the CLC2006 product is about 70% at the classification level where the forested area is separated into three main groups: Deciduous, coniferous and mixed. At the next level, these groups were also classified according to the ground conditions: On mineral soil, on peat land and on rocky shore. The database used in this work is in this classification level. The accuracy is not specified at this level; however, it is expected

to be lower than 70%. Therefore, confusion in the forest classes will be the most important factor which will decrease the accuracy of the analysis which is based on the forest classes.

5. Results and Discussion

In this chapter, the results of the forest class-dependent temporal variability analysis are presented. Comparisons are made about the relevant parameters and their temporal variations and the results are discussed. Section 5.1 presents the results and the discussion of our analysis made on HH-pol dataset. Section 5.2, on the other hand, presents the results of the same analysis made on VV-pol dataset and also makes comparison between VV-pol and HH-pol dependencies.

5.1 HH-Pol Acquisitions

This section presents and discusses the results of forest type-specific temporal variation analysis applied to the HH-pol SAR data. In Subsection 5.1.1, the parameter of the interest is interferometric coherence magnitude. In Subsection 5.1.2, the other three parameters (SPC height, penetration depth and relative location of SPC to the treetop) are considered since these three are actually not independent of each other.

5.1.1 Temporal Variations in Interferometric Coherence with respect to Forest Type

Section 4.1 described the method that is used to produce interferometric coherence magnitude maps. For all five HH-pol TanDEM-X/TerraSAR-X datasets, the method is applied and coherence maps are obtained. Average coherence values and the standard deviation of the coherence values for dominant forest classes in CLC2006 database are calculated for each map as described in 4.2.3. In order to map the patterns and variations clearly and more visually, results are presented in both table and line format. Table 5.1, Table 5.2, Figure 5.1 and Figure 5.2 present the results of our analysis.

Table 5.1 HH-pol mean of coherence magnitude with respect to forest class and date of acquisition.

		Date of Acquisition				
		Sep. 4	Sep. 15	Oct. 18	Oct. 29	Nov. 9
Forest Class	Deciduous	0.894	0.827	0.851	0.872	0.863
	Coniferous	0.864	0.808	0.823	0.839	0.826
	Mixed	0.886	0.818	0.842	0.862	0.851

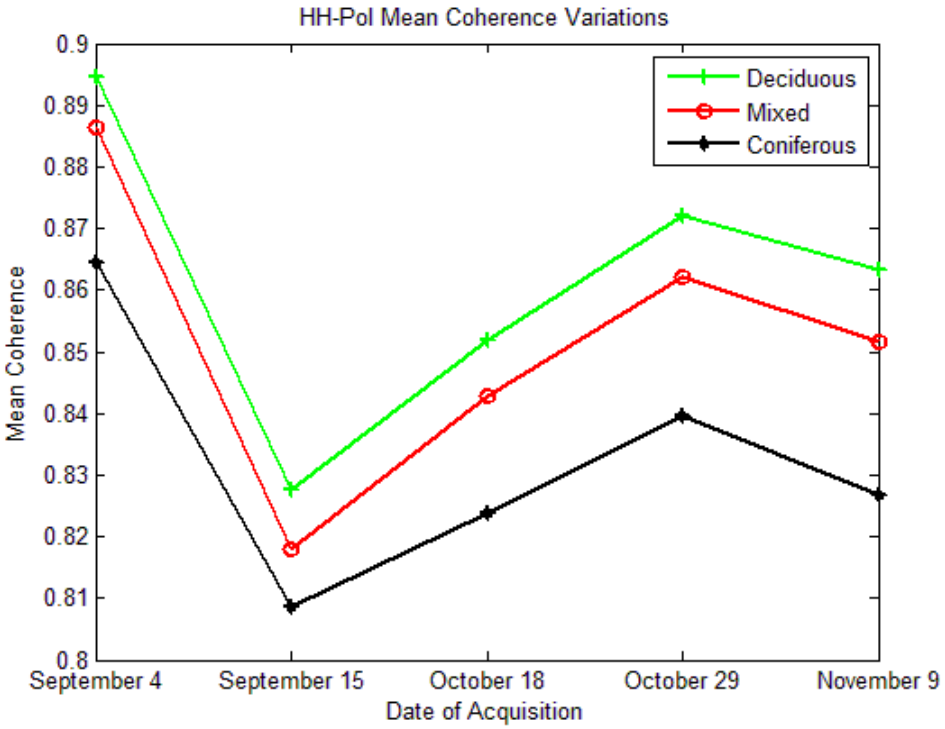

Fig 5.1 HH-pol mean of coherence magnitude with respect to forest class and date of acquisition.

Table 5.2 Standard deviation of coherence magnitude with respect to forest class and date of acquisition.

		Date of Acquisition				
		Sep. 4	Sep. 15	Oct. 18	Oct. 29	Nov. 9
Forest Class	Deciduous	0.04	0.073	0.044	0.038	0.038
	Coniferous	0.063	0.089	0.064	0.059	0.067
	Mixed	0.049	0.084	0.052	0.049	0.053

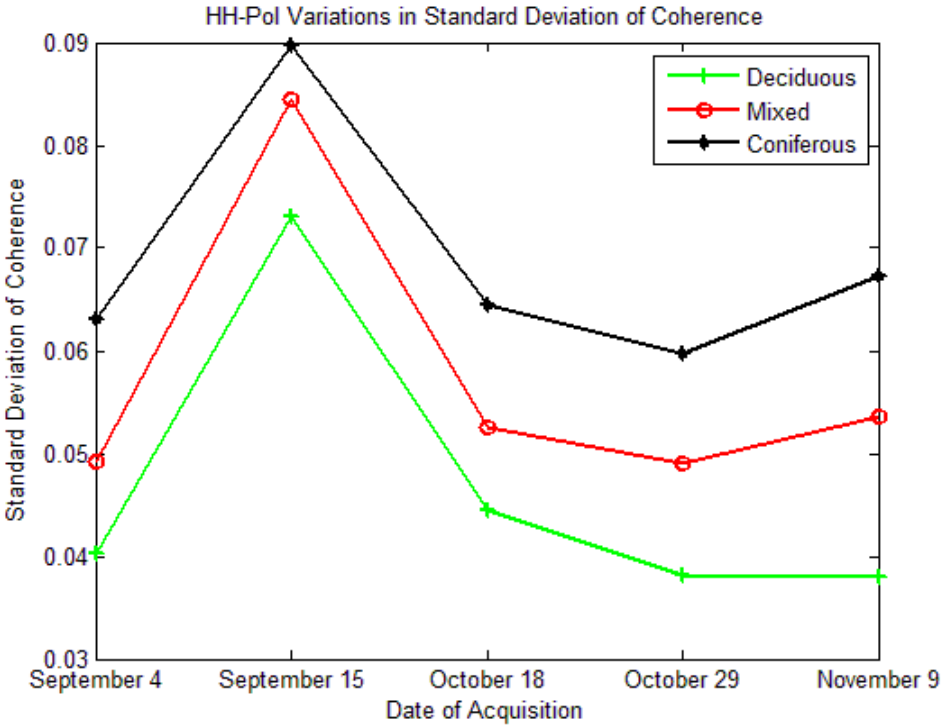

Fig 5.2 Standard deviation of coherence magnitude with respect to forest class and date of acquisition.

Figures and Tables 5.1 and 5.2 illustrate that:

- Average coherence is always highest for deciduous forest and lowest for coniferous forest.
- Standard deviation of the coherence values is always highest for coniferous forest and lowest for deciduous forest.

- The acquisition on September 15 is highly affected by the phase noise which increased its standard deviation of coherence values.

- If average coherence increases from one acquisition to another, standard deviation decreases and vice versa.

As explained in Subsection 2.3.4, only target dependent decorrelation in TanDEM-X/TerraSAR-X pair is volume decorrelation. In other words, the differences between the coherence statistics of distinct forest classes are related to the strength of the volume scattering. Obviously in every acquisition, volume scattering is most significant for coniferous forest while it is the least effective in deciduous trees. Highest temporal variations are recorded for deciduous and mixed forest, which can be considered as the result of the leaf/needle drop which takes place during autumn. At this point it is not reasonable to comment on temporal variability more because each coherence set is affected differently by the target-independent decorrelation $|C|_{ambiguity}|C|_{quantization}|C|_{SNR}$, therefore it is really hard to retrieve the exact values for volume decorrelation. Also, analyzing the weather conditions during each acquisition, high decorrelation in the data acquired on September 15, 2011 must be related to the rainy conditions of the previous days since water over the surfaces have decorrelating effect. Higher standard deviation values of the coniferous forest shows the less homogeneous structure of the forest and its distribution on land.

5.1.2 Temporal Variations in SPC Height and Related Statistics with respect to Forest Type

Five sets of HH-pol TanDEM-X/TerraSAR-X data are processed using the interferometric chain described in Chapter 4. CHM for each set is obtained. Figures 5.3 - 5.8 illustrate the CHM maps obtained by SAR and the LIDAR.

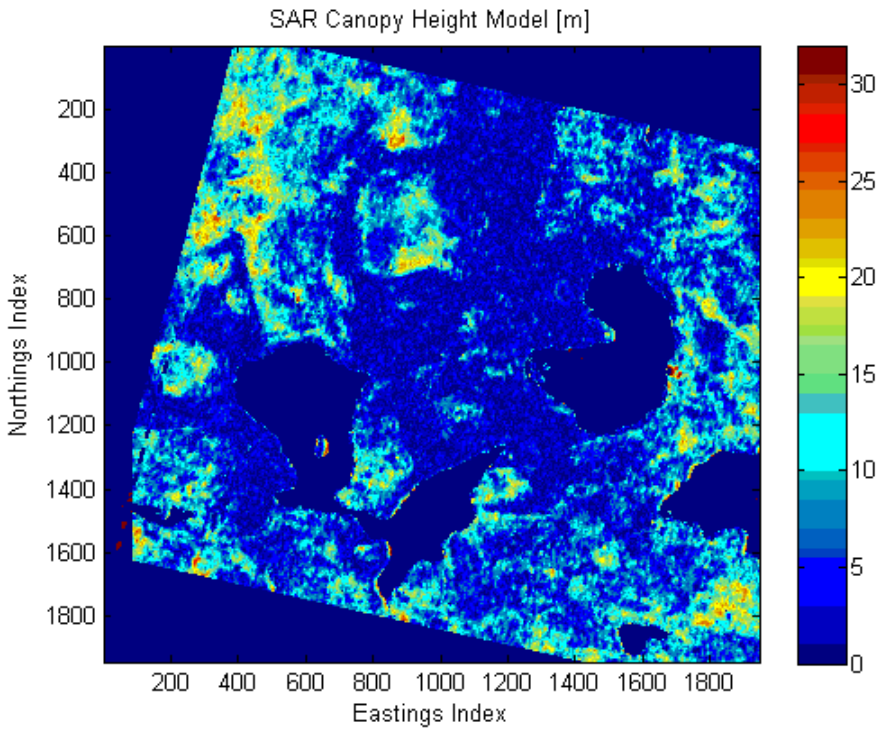

Fig 5.3 CHM retrieved by the data obtained on September 4, 2011.

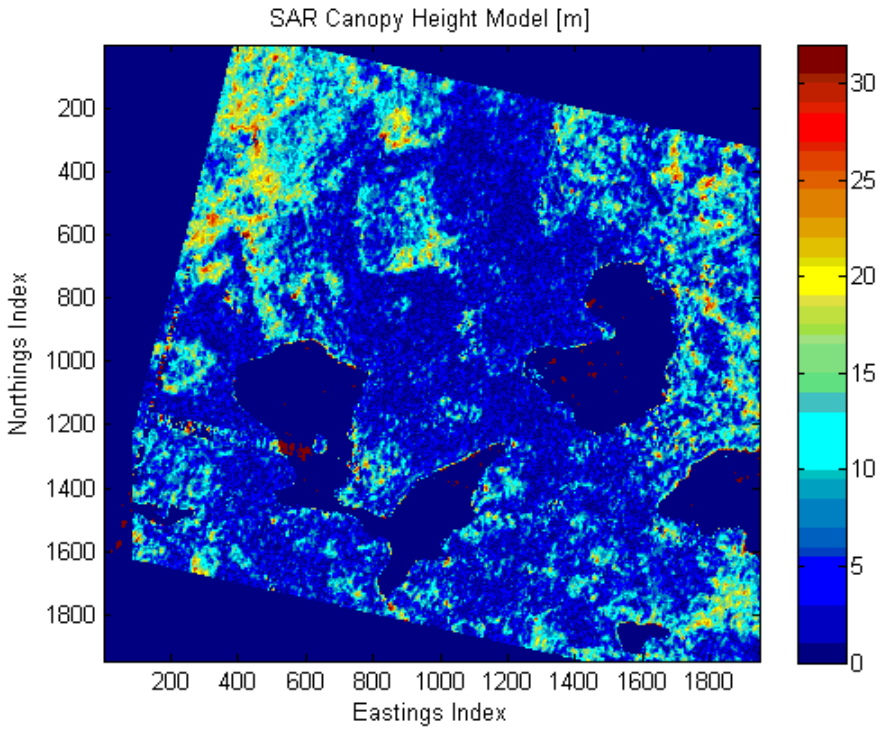

Fig 5.4 CHM retrieved by the data obtained on September 15, 2011.

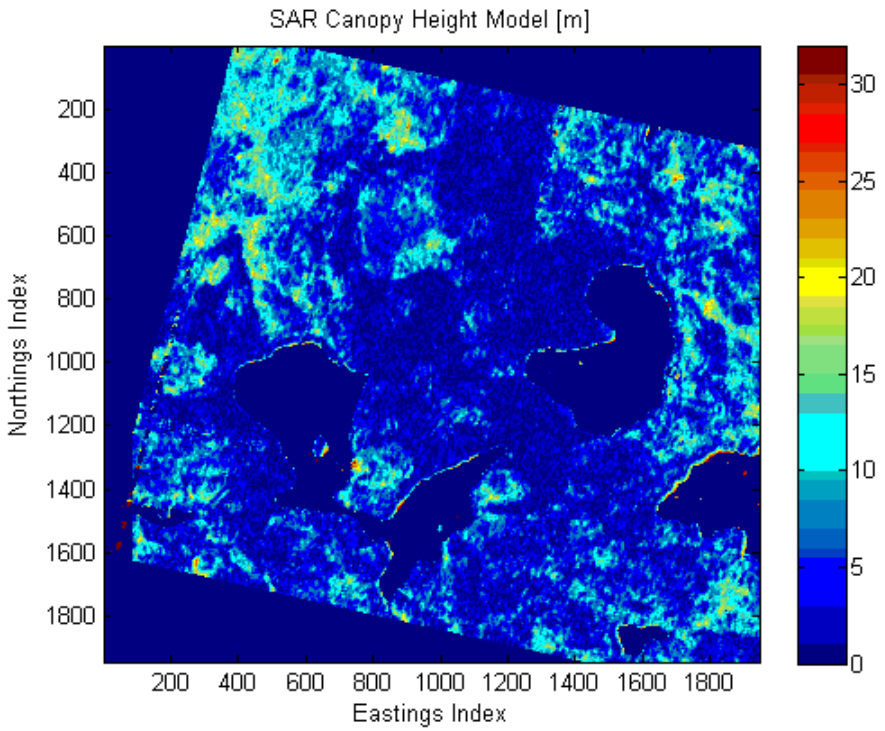

Fig 5.5 CHM retrieved by the data obtained on October 18, 2011.

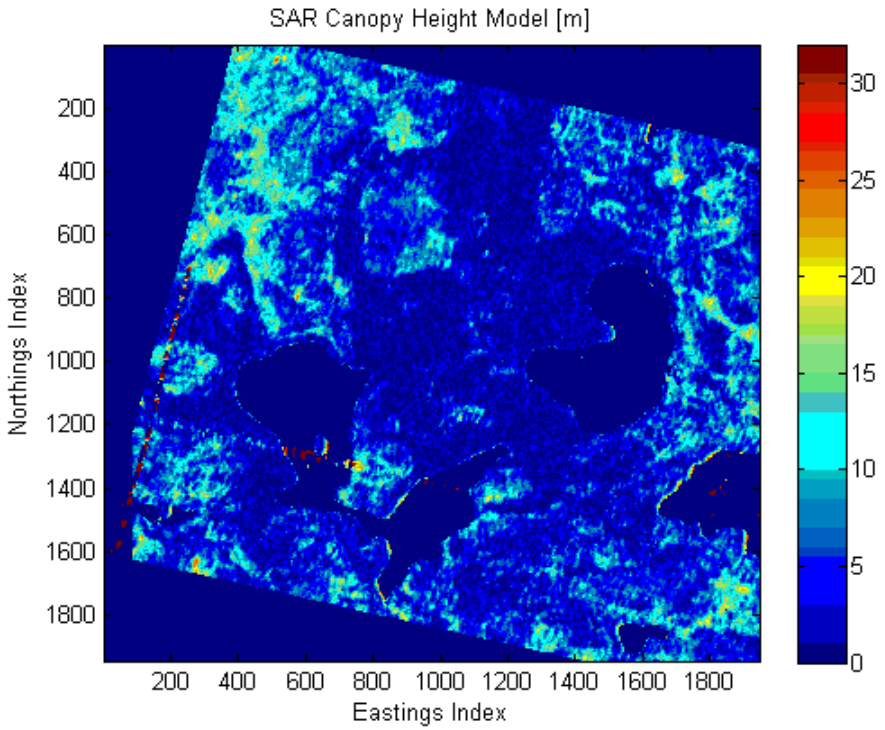

Fig 5.6 CHM retrieved by the data obtained on October 29, 2011.

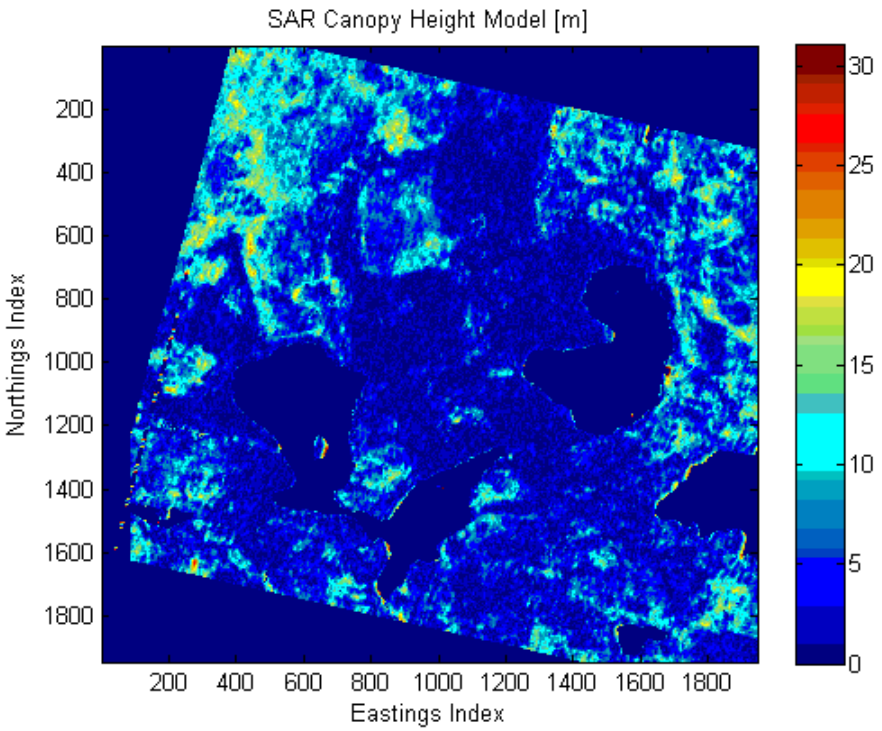

Fig 5.7 CHM retrieved by the data obtained on November 9, 2011.

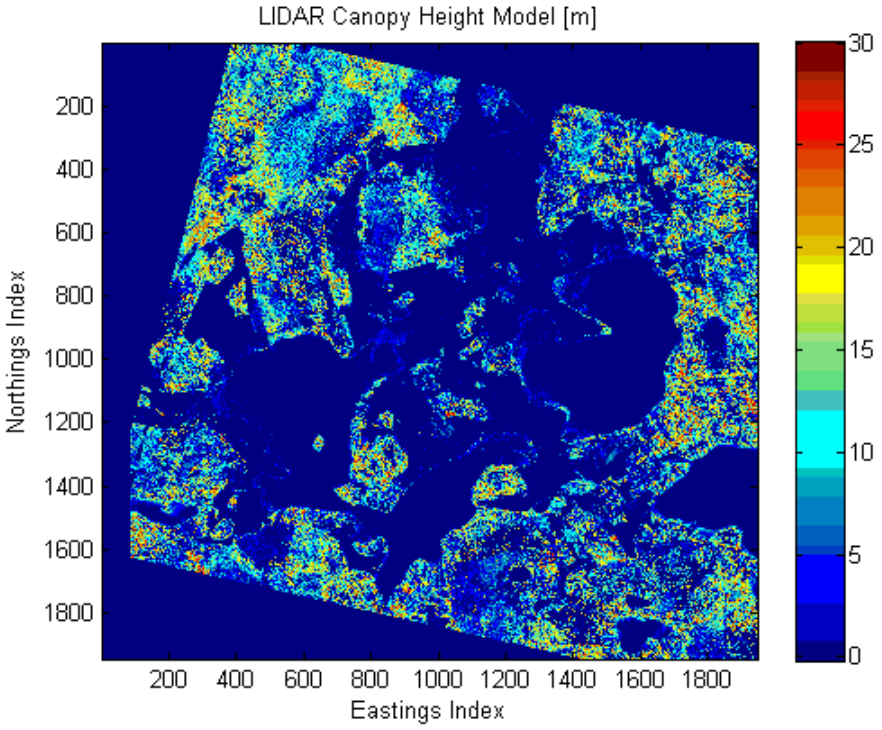

Fig 5.8 LIDAR measured CHM.

Figures 5.3 - 5.8 illustrate that:

- The 5 CHMs produced by SAR interferometric chain follow a similar pattern; however, the acquisitions in September produced a CHM with higher tree heights than acquisitions in October and December.

- SAR CHMs also follow a similar pattern with LIDAR CHM; however, the sensitivity of SAR to the canopy height variations is lower than that of LIDAR.

- Smoothness of SAR produced CHMs depends on the average coherence of the interferogram or simply the SNR. Higher noise in the interferogram causes higher decrease in average coherence, thus less smooth CHM. The highest decorrelation was found in the data acquired on September 15, 2011; therefore the noise contribution to CHM is more and reducing the smoothness.

- An indicator of the noisy conditions is the amount of the reddest point in the CHM, since the retrieved tree heights higher than 32 m is equalized to 32 m. Acquisition on September 15, 2011 has the biggest amount of reddest points.

The CLC2006 Finnish Land Classification map includes three dominant classes of forest: Deciduous forest on mineral soil, coniferous forest in mineral soil, mixed forest in mineral soil. Pixelwise for each class, the parameters mean SPC height, mean penetration depth and mean relative location of SPC to the treetop is calculated. Subsection 4.2.3 presented how these parameters are defined and calculated. Result of the mean SPC height analysis is presented in Table 5.3 and Figure 5.9.

Table 5.3 Mean SPC heights [m] with respect to acquisition date and forest class (HH-pol).

		Date of Acquisition				
		Sep. 4	Sep. 15	Oct. 18	Oct. 29	Nov. 9
Forest Class	Deciduous	9.79	8.75	6.88	6.35	6.58
	Coniferous	9.19	8.57	7.18	7.01	7.06
	Mixed	9.16	8.23	6.49	6.13	6.22

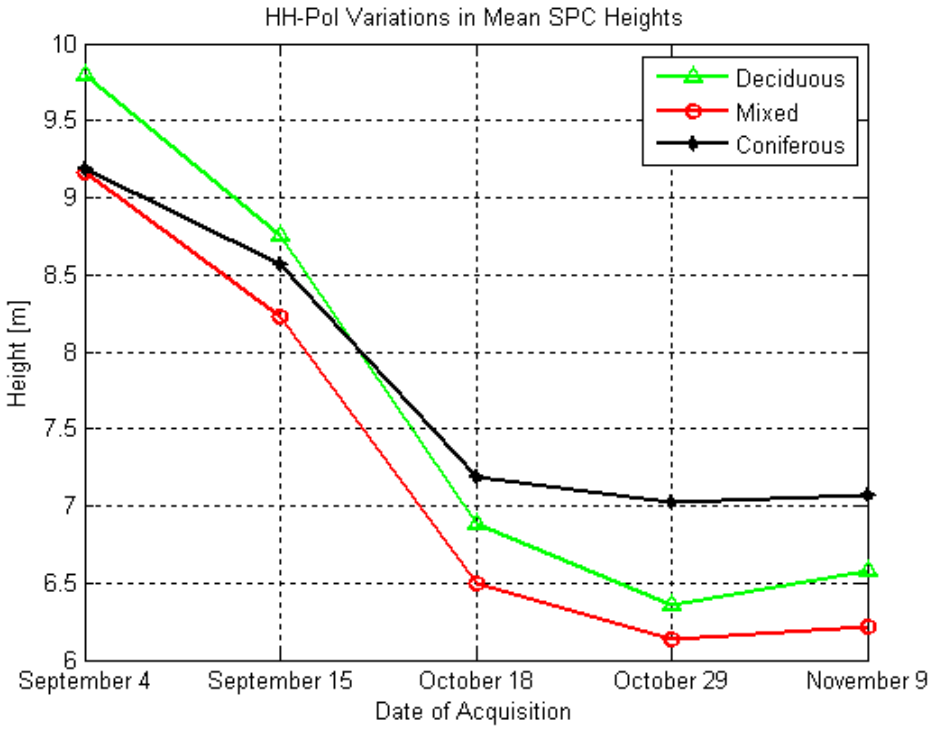

Figure 5.9 Mean SPC heights with respect to acquisition date and forest class (HH-pol).

Figure 5.9 and Table 5.3 show that:

- In September acquisitions average SPC height is highest for deciduous forest, lowest for mixed forest and coniferous forest comes in the middle.
- In October and November acquisitions, average SPC height is highest for coniferous forest, lowest for mixed forest and deciduous forest comes in the middle.
- There is a gradual decrease in the retrieved average tree heights from September 4 acquisition until October 29 acquisition, and then a small increase from October 29 acquisition to November acquisition.
- The biggest variation in mean SPC heights occurred in the interval between September 15 and October 18.

- The highest decrease in average SPC heights during autumn is observed in deciduous forest type which is equal to 3.44 meters. The decrease was 3.03 meters for mixed forest and only 2.17 meters for coniferous forest.
- Average SPC height for mixed forest is always the lowest within the three classes.

Gradual decrease in the mean SPC heights is caused by the leaf and needle drop and color change which starts in early September and continues until November. The change in the average retrieved tree heights between October 18 and November 9 acquisitions is small in comparison to the change from September to October which indicates the major leaf drop have occurred during from early September to mid-October. Deciduous trees (alder and birch in test site) are known to drop their leaves during autumn. Coniferous forest on the contrary is known to keep most of their needles during winter. However, it has been reported that Scots pine also drop or lose their needles periodically [57] or diseases can cause needle loss in Norway spruce [58]. Also the accuracy of the CLC2006 land classification map is less than 70%, thus we expect confusion in forest type classification. As a consequence, gradual drop in coniferous forest statistics are also expected. For these reasons, it is expected that highest temporal drop in average SPC height would belong to the deciduous forest and lowest to the coniferous forest. Since mixed forest can be considered as the mix of coniferous and deciduous kinds, the drop in the SPC is expected to be between. That is exactly what is observed in our analysis of TanDEM-X/TerraSAR-X data. The small increase in the mean SPC heights from October 29 to November 9 can be related to the big temperature drop between those dates since other weather conditions are quite similar. During the October acquisition, the temperature recorded was 10^{o} C. During the November acquisition, the temperature recorded was -1^{o} C which decreased the dielectric constant of the forest, and as a consequence, reflection from canopy and the SPC heights were increased.

The observation that average SPC height is always lowest for mixed forest does not contradict with the observations about temporal variations since average SPC height is affected by individual tree heights and the density of the forest. Mixed forest of the

test site can be sparser than coniferous and deciduous or can be denser with lower individual tree heights. However, it is not possible to deduct the exact reason.

Mean penetration depth was another parameter that is examined. Table 5.4 and its line format equivalent Figure 5.10 present the result of the analysis.

Table 5.4 Mean penetration depths [m] with respect to SAR acquisition date and forest class (HH-pol).

		Date of Acquisition				
		Sep. 4	Sep. 15	Oct. 18	Oct. 29	Nov. 9
Forest Class	Deciduous	2.52	3.63	6.01	6.77	6.3
	Coniferous	5.01	5.77	7.32	7.47	7.34
	Mixed	3.68	4.89	6.93	7.39	7.2

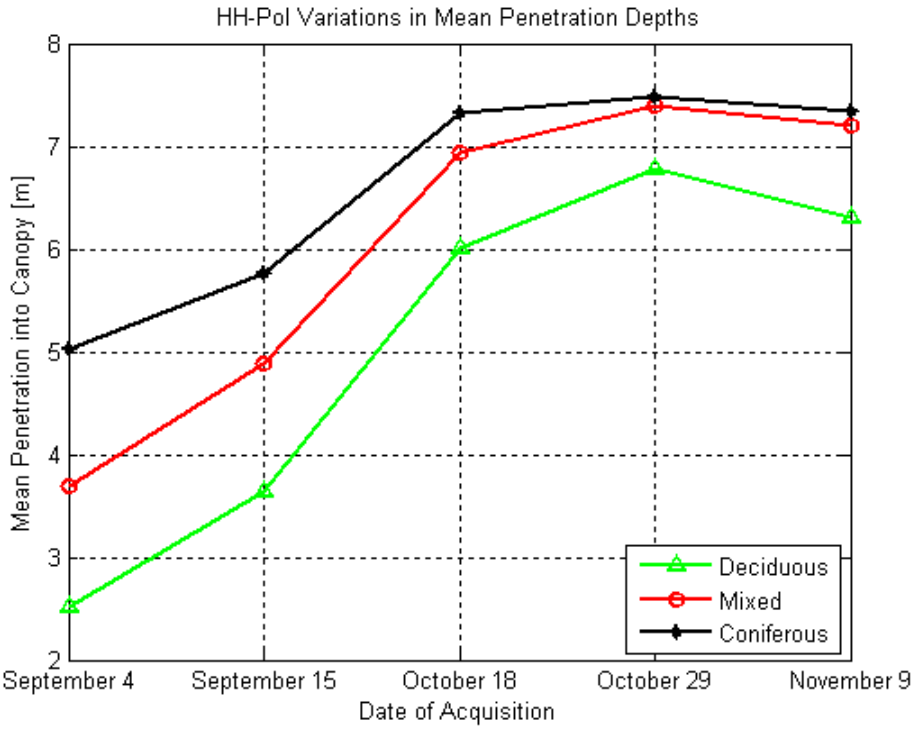

Figure 5.10 Mean penetration depths [m] with respect to SAR acquisition date and forest class (HH-pol).

Figure 5.10 and Table 5.4 show that:

- The average penetration depth into canopy is lowest for September 4 and highest for October 29 acquisitions for all forest classes.
- There is a gradual increase in average penetration depths from September 4 until October 29, and a small decrease from October 29 to November 9.
- Average penetration depth for coniferous forest is always the highest within the forest classes on each acquisition. It is always the lowest for deciduous forest, and for mixed forest, it is in between the values of deciduous and coniferous forest. SPC height and penetration depth are independent parameters, results about penetration depth statistics do not contradict with SPC height statistics.
- The biggest change in the mean penetration depths occurred in the interval between September 15 and October 18.
- The highest increase (4.25 meters) in the mean penetration depth is observed for deciduous forest, the lowest increase (2.46 meters) belongs to coniferous forest and the increase in mixed forest mean penetration (3.70 meters) comes in the middle (in the time interval between September 4 and October 29).
- Differences in the mean penetration depths of classes are highest at September 4, and then it gradually decreases until October 29.

The pattern observed in the temporal variations of mean penetration is in total agreement with the temporal variability of the SPC height statistics. Leaf-on conditions of early September and middle September resulted in lower penetration depths since the X-band SAR signals are strongly attenuated by the leaves and needles. Again the mean penetration depth variation for all classes is highest from September 4 to October 18 which indicates that major part of leaf or needle drop occurred in this interval. Deciduous forest has the most sensitive penetration depth statistics since it is the class most affected by leaf drop. Coniferous forest penetration depth has the lowest temporal variations as expected. One interesting observation about the average penetration depth is that, even though deciduous forest loses its leaves during autumn, the average penetration is still lower than that for coniferous

forest in November acquisition. This observation suggests that the deciduous forest in the test site is relatively dense and branches are effective scattering elements in absence of leaves. The accuracy of penetration depth statistics are also affected by the accuracy of the CLC2006 database as observed in SPC height statistics.

The final parameter analyzed for HH-pol SAR data is the relative location of SPC to the treetop. Assuming LIDAR measured CHM is 100% accurate, the treetop heights are directly taken from LIDAR CHM. SPC heights, on the other hand, directly comes from the CHMs presented in Figures 5.3 – 5.7. This ratio is useful to analyze since it is directly related to the structure and the specie of the forest. Also, it provides a better opportunity to making comparisons between forest classes. Figure 5.11 and Table 5.5 show the outcome of the temporal variation analysis.

Table 5.5 Mean relative location of SPC to the treetop with respect to SAR acquisition date and forest class (HH-pol)

		Date of Acquisition				
		Sep. 4	Sep. 15	Oct. 18	Oct. 29	Nov. 9
Forest Class	Deciduous	0.874	0.799	0.639	0.589	0.626
	Coniferous	0.71	0.662	0.558	0.548	0.557
	Mixed	0.794	0.715	0.576	0.546	0.559

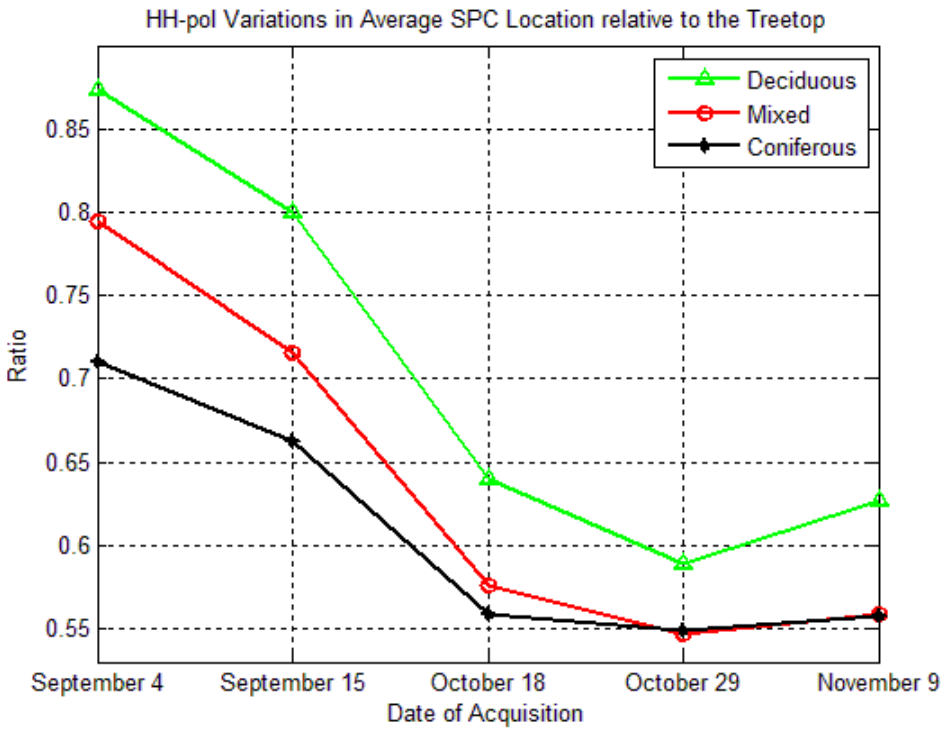

Figure 5.11 Mean relative location of SPC to the treetop with respect to SAR acquisition date and forest class (HH-pol).

Figure 5.11 and Table 5.5 show that:

- The average relative location of SPC to the treetop is highest for September 4 and lowest for October 29 acquisition for all forest classes.
- For all forest classes, gradual decrease in the parameter is observed from September 4 until October 29. There is a small increase from October to November acquisition.
- For all acquisitions, deciduous forest yield highest mean relative location of SPC to the treetop and coniferous forest yield the lowest. In September acquisitions, the parameter for mixed forest is almost the average of deciduous and coniferous parameters; however in October and November acquisitions, the parameter is almost the same for mixed and coniferous forest.
- Highest variation in mean relative location of SPC to the treetop took place in the interval between September 15 and October 18.

- The highest decrease (28.47%) in mean relative location of SPC to the treetop is observed for deciduous forest, lowest decrease (17.16%) belongs to coniferous forest and the decrease in mixed forest parameter (24.74%) is between them (between September 4 and October 29).

- Within the forest classes, highest differences between parameters are observed in September 4 acquisition and the lowest in October 29.

Results are totally in agreement with the variations observed in SPC height and penetration depth statistics. The phenomenon behind the variations is basically the same for each parameter analyzed in this section.

5.2 VV-Pol Acquisitions

In this section, the results obtained with VV-pol SAR images are presented and discussed. In Subsection 5.2.1 interferometric coherence is the parameter of interest and in Subsection 5.2.2 SPC height, penetration depth and relative location of SPC to the treetop are the focuses. Also in both subsections, comparison of VV-pol and HH-pol results are made.

5.2.1 Temporal Variations in Interferometric Coherence with Respect to Forest Type

VV-pol dataset are also processed by the same algorithms and methods with HH-pol dataset. Figure 5.12 and Table 5.6 present the temporal changes of average coherence with respect to forest classes. Figure 5.13 and Table 5.7, on the other hand, illustrate the temporal changes in standard deviation of the coherence magnitude depending on the forest classes.

Table 5.6 VV-pol mean of coherence magnitude with respect to forest class and date of acquisition

		Date of Acquisition				
		Sep. 4	Sep. 15	Oct. 18	Oct. 29	Nov. 9
Forest Class	Deciduous	0.895	0.83	0.851	0.875	0.864
	Coniferous	0.862	0.814	0.825	0.846	0.832
	Mixed	0.884	0.822	0.843	0.866	0.854

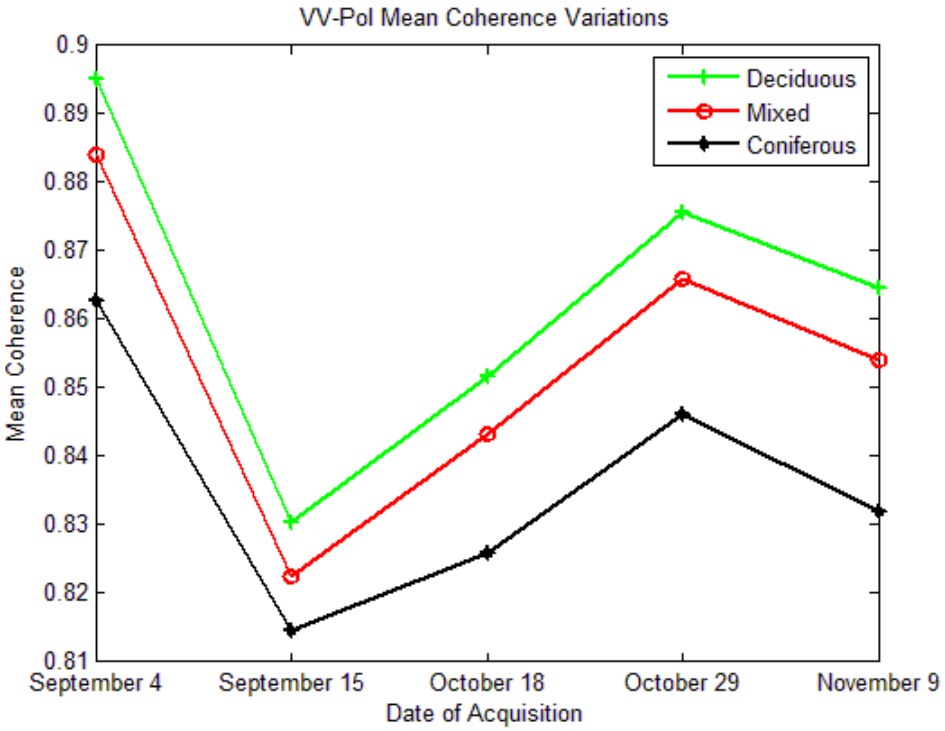

Fig 5.12 VV-pol mean of coherence magnitude with respect to forest class and date of acquisition.

Table 5.7 Standard deviation of coherence magnitude with respect to forest class and date of acquisition.

		Date of Acquisition				
		Sep. 4	Sep. 15	Oct. 18	Oct. 29	Nov. 9
Forest Class	Deciduous	0.043	0.072	0.042	0.032	0.036
	Coniferous	0.062	0.084	0.061	0.055	0.063
	Mixed	0.051	0.079	0.051	0.044	0.046

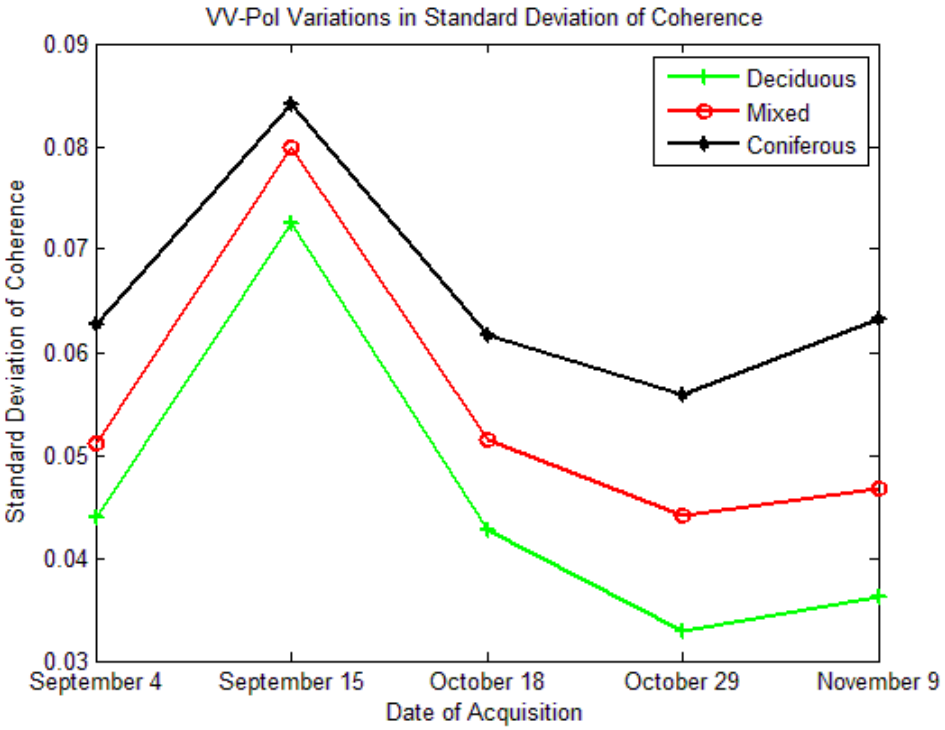

Fig 5.13 VV-pol standard deviation of coherence magnitude with respect to forest class and date of acquisition.

Compared to the HH-pol results, the exactly the same observations can be made about the observed temporal variations with respect to each forest class. For each acquisition and for each forest class, the difference in VV-pol and HH-pol averages are very small (maximum ~ 0,004). Mostly, VV-pol mean coherence values are higher and standard deviation values are lower than HH-pol. However, it is not clear that whether the differences are caused by different volume decorrelation $|C|_{volume}$ or the target-independent decorrelation $|C|_{ambiguity}|C|_{quantization}|C|_{SNR}$.

5.2.2 Temporal Variations in SPC Height and Related Statistics with respect to Forest Type

As already done for HH-pol dataset, five sets of VV-pol TanDEM-X/TerraSAR-X data are processed with the same interferometric methodology. CHM for each set is

obtained. CHM obtained by each VV-pol data has shown very similar properties with its twin HH-pol data. Therefore, the same comments about the HH-pol CHMs (see Page 59) can be made for VV-pol CHMs. Differences between HH-pol and VV-pol CHMs are to be made clear after comparing the SPC height statistics. VV-pol CHMs are presented in Figures 5.14 - 5.18.

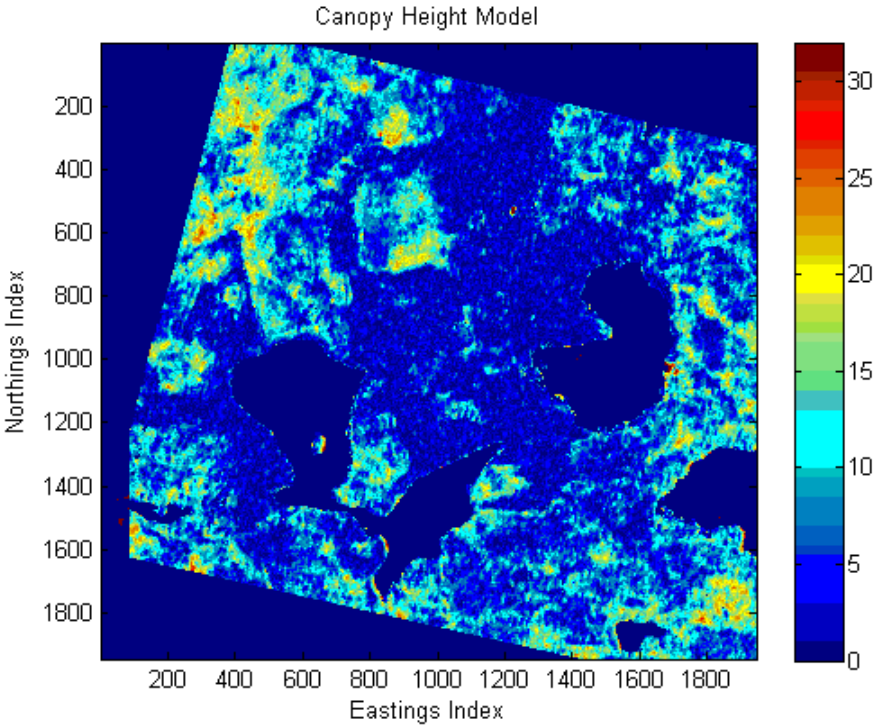

Figure 5.14 CHM (VV-pol) retrieved by the data obtained on September 4, 2011.

Unit of the colorbar is meters.

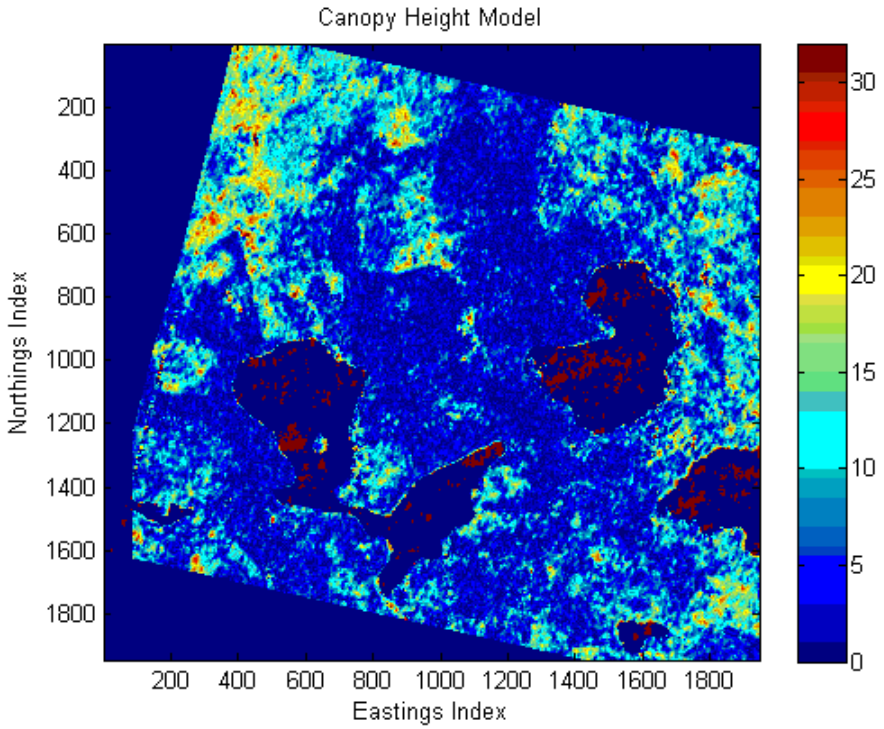

Figure 5.15 CHM (VV-pol) retrieved by the data obtained on September 15, 2011. *Unit of the colorbar is meters.*

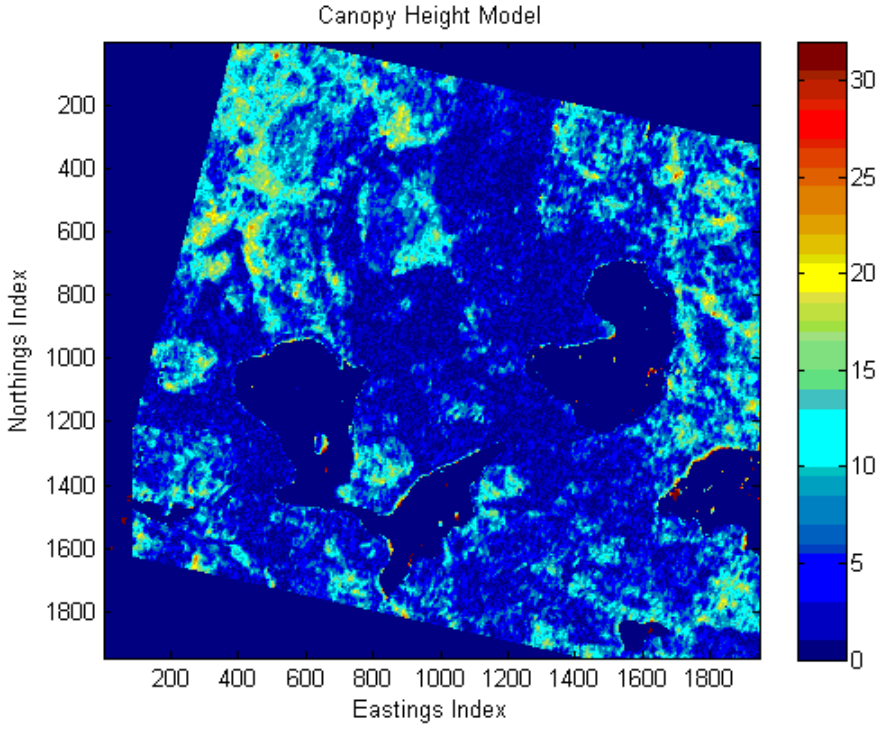

Figure 5.16 CHM (VV-pol) retrieved by the data obtained on October 18, 2011. *Unit of the colorbar is meters.*

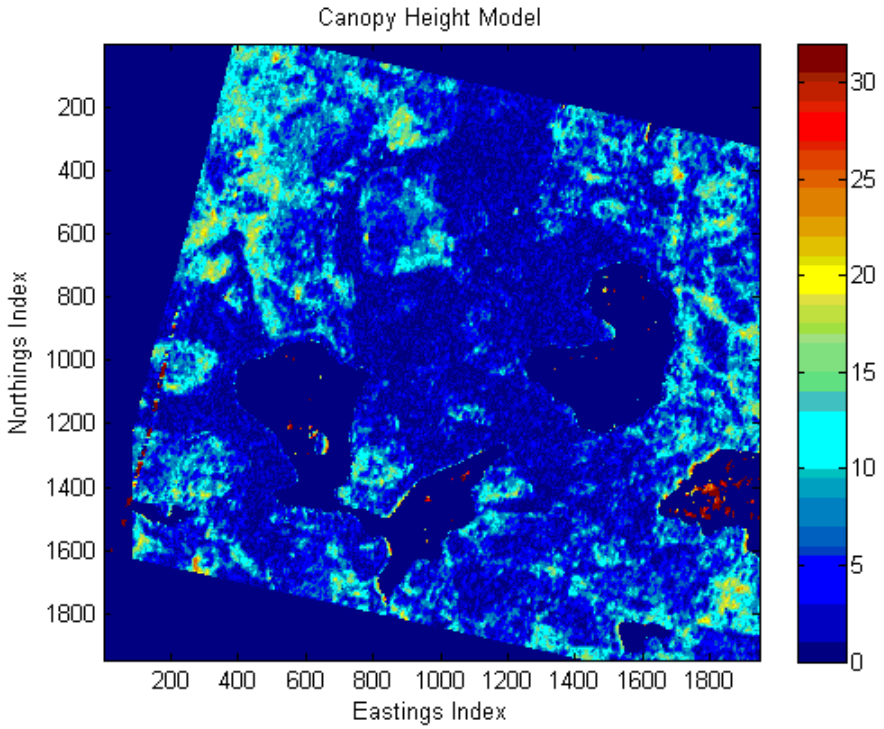

Figure 5.17 CHM (VV-pol) retrieved by the data obtained on October 29, 2011. *Unit of the colorbar is meters.*

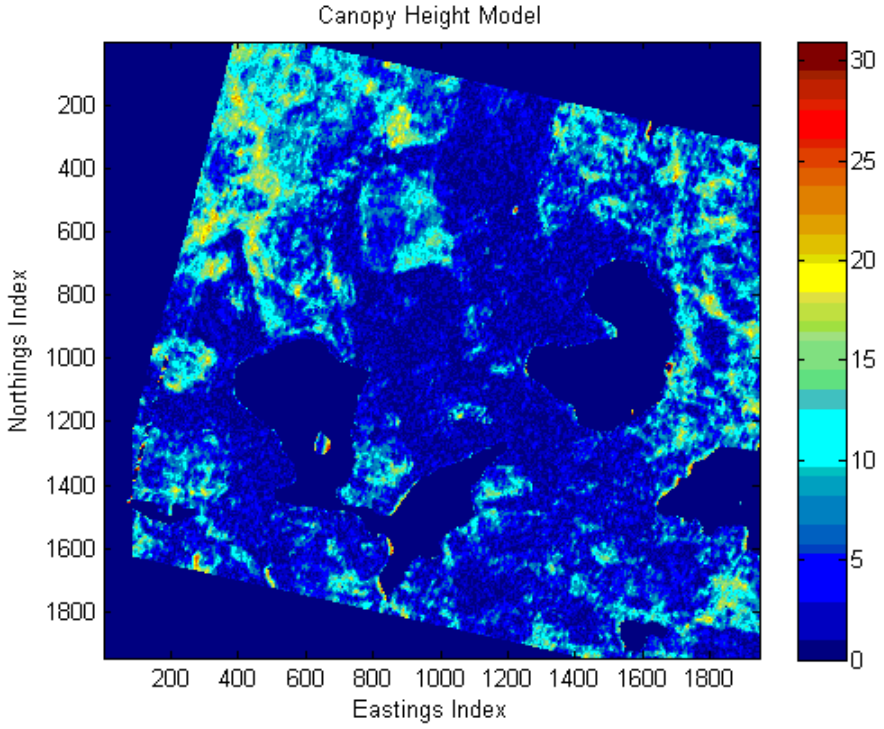

Figure 5.18 CHM retrieved by the data obtained on November 9, 2011. *Unit of the colorbar is meters.*

For each VV-pol dataset, the same parameters as in Subsection 5.1.2 are analyzed. Table 5.8 and Figure 5.19 show the results of the mean SPC height analysis. Table 5.9 and Figure 5.20 present the temporal variations in mean penetration depth with respect to forest class. Finally, Table 5.10 and Figure 5.21 give the result of relative location of SPC to the treetop analysis.

Table 5.8 Mean SPC heights [m] with respect to acquisition date and forest class (VV-pol).

		Date of Acquisition				
		Sep. 4	Sep. 15	Oct. 18	Oct. 29	Nov. 9
Forest Class	Deciduous	9.9	9.46	7.43	7.01	7.14
	Coniferous	9.43	9.05	7.78	7.56	7.43
	Mixed	9.22	8.7	7.08	6.66	6.72

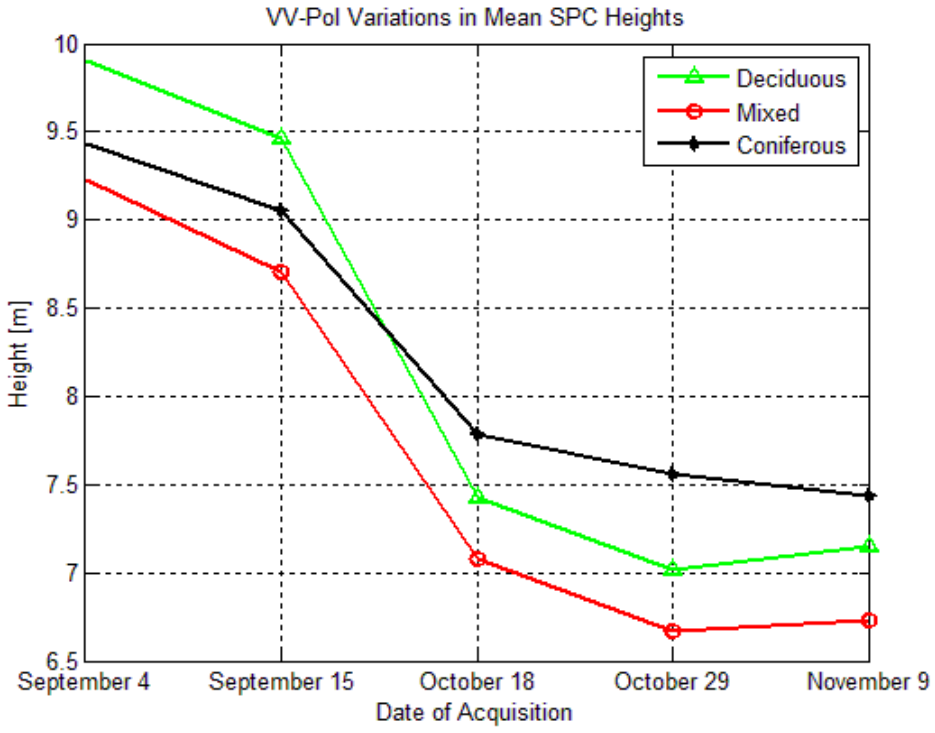

Figure 5.19 Mean SPC heights [m] with respect to SAR acquisition date and forest class (VV-pol).

Table 5.9 Mean penetration depths [m] with respect to SAR acquisition date and forest class (VV-pol).

		Date of Acquisition				
		Sep. 4	Sep. 15	Oct. 18	Oct. 29	Nov. 9
Forest Class	Deciduous	2.29	2.89	5.33	5.82	5.53
	Coniferous	4.64	5.2	6.52	6.8	6.85
	Mixed	3.56	4.27	6.19	6.65	6.49

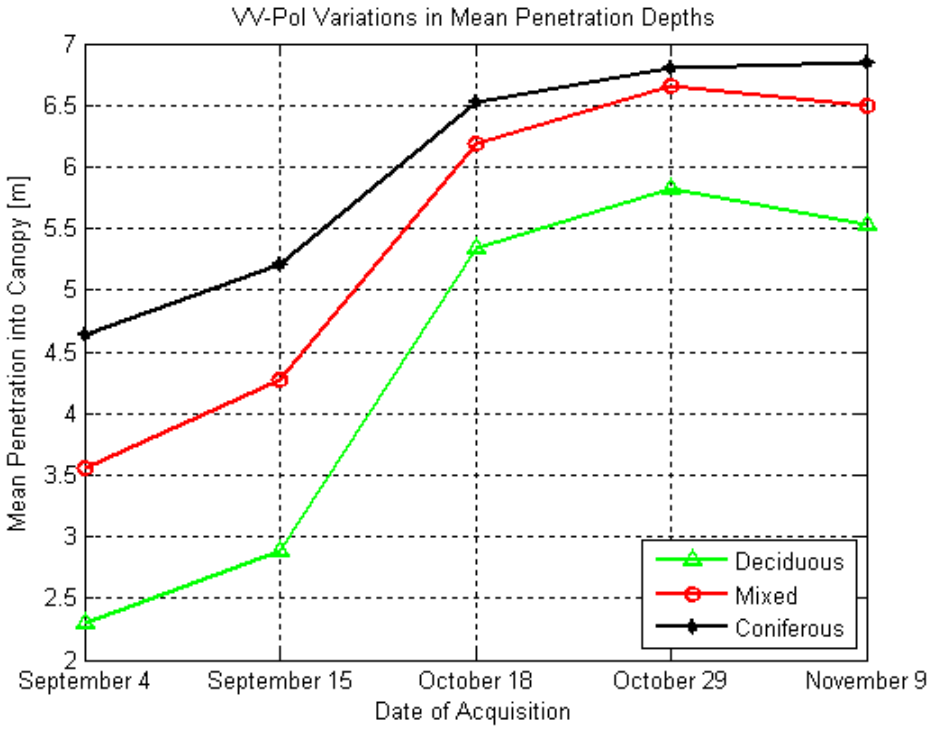

Figure 5.20 Mean penetration depths [m] with respect to SAR acquisition date and forest class (VV-pol).

Table 5.10 Mean relative location of SPC to the treetop with respect to SAR acquisition date and forest class (VV-pol).

		Date of Acquisition				
		Sep. 4	Sep. 15	Oct. 18	Oct. 29	Nov. 9
Forest Class	Deciduous	0.887	0.849	0.684	0.652	0.671
	Coniferous	0.733	0.699	0.61	0.591	0.589
	Mixed	0.802	0.755	0.625	0.595	0.605

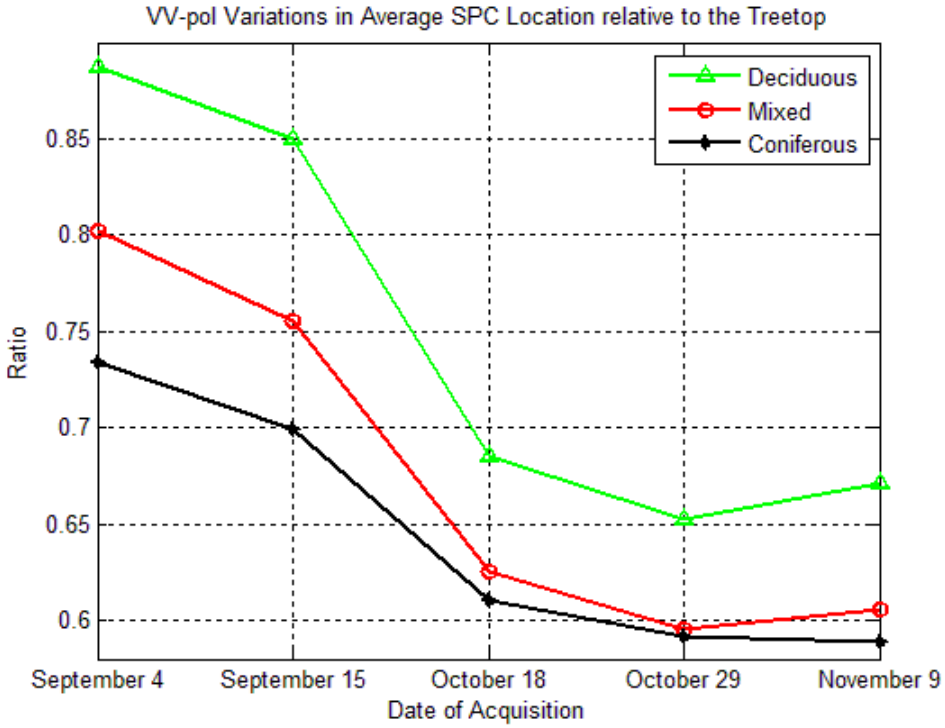

Figure 5.21 Mean relative location of SPC to the treetop with respect SAR acquisition date and forest class (VV-pol).

Figures 5.19-5.21 and Tables 5.8-5.10 illustrate that VV-pol temporal variations in three parameters of our interest are almost identical with HH-pol with the exception:

- For coniferous forest, VV-pol variations in the parameters from October 29 to November 9 are in the opposite way of HH-pol variations. Specifically, mean

penetration has increased in this time interval for VV-pol acquisitions while it has decreased for HH-pol acquisitions.

For all forest classes and acquisitions:

- VV-pol mean SPC height is always larger than HH-pol mean SPC height for the same acquisition date. The difference between these parameters is the lowest for the September 4 acquisition.
- VV-pol average penetration depth is always higher than HH-pol average penetration depth for the same SAR acquisition.
- VV-pol mean relative location of SPC to the treetop is always higher than the HH-pol equivalent for the same SAR acquisition.

VV-pol signals are attenuated more by the forest canopy and also specular scattering of ground surface at HH polarization is stronger than that at VV polarization since Fresnel reflection coefficient is positive at VV polarization before the incidence angle becomes the same with Brewster angle whereas it is negative for HH polarization [24], therefore higher SPC height is expected for VV polarization. Our results confirmed the phenomenon. Another observation about the differences between VV-pol and HH-pol statistics is that the highest statistical variations during the time interval between the first and the last acquisition are observed in HH-pol retrieved parameters. Below, for each forest class, the highest changes in the relevant parameters are presented which were mostly observed between September 4 and October 29 acquisitions:

For coniferous forest:

- VV-pol highest decrease in mean SPC height is 1.99 meters.
- HH-pol highest decrease in mean SPC height is 2.17 meters.
- VV-pol highest increase in mean penetration is 2.21 meters.
- HH-pol highest increase in mean penetration is 2.46 meters.
- VV-pol highest decrease in mean relative location of SPC to the treetop is 15.44%.

- HH-pol highest decrease in mean relative location of SPC to the treetop is 17.16%.

For deciduous forest:

- VV-pol highest decrease in mean SPC height is 2.88 meters.
- HH-pol highest decrease in mean SPC height is 3.44 meters
- VV-pol highest increase in mean penetration is 3.52 meters.
- HH-pol highest increase in mean penetration is 4.25 meters.
- VV-pol highest decrease in mean relative location of SPC to the treetop is 23.45%.
- HH-pol highest decrease in mean relative location of SPC to the treetop is 28.47%.

For mixed forest:

- VV-pol highest decrease in mean SPC height is 2.56 meters.
- HH-pol highest decrease in mean SPC height is 3.03 meters.
- VV-pol highest increase in mean penetration is 3.09 meters.
- HH-pol highest increase in mean penetration is 3.70 meters.
- VV-pol highest decrease in mean relative location of SPC to the treetop is 20.7%.
- HH-pol highest decrease in mean relative location of SPC to the treetop is 24.74%.

All parameters showed higher temporal variations for HH-pol SAR CHM than VV-pol. Therefore it can be concluded that HH polarization is more sensitive to the changes in the forest canopy such as leaf or needle drop. For mapping temporal variability, forest classification algorithms and such applications, HH-pol SAR data include more distinctive information than the VV-pol.

6. Conclusions and Future Work

In the final chapter of the thesis, conclusions are presented at Section 6.1 and some suggestions about future work are made on Section 6.2.

6.1 Conclusions

The thesis work intended to explore the capability of X-band spaceborne interferometric radar to monitor temporal variability in forest. To this end, 5 sets of dual polarimetric (HH/VV) TanDEM-X CoSSC products were interferometrically processed. For each set, Canopy Height Model (CHM) was derived from interferometric coherence phase using LIDAR Digital Terrain Model (DTM) as the auxiliary data. Using the LIDAR CHM and the land cover CLC2006 data, temporal variations in average Scattering Phase Center (SPC) heights, penetration depths and relative location (ratio) of SPC to the treetop were mapped with respect to coniferous, deciduous and mixed forest classes.

For each forest class, the mean SPC height and its relevant location to the treetop was found to be decreasing from early September until late October. Since penetration depth and SPC heights are inversely proportional parameters, mean penetration was increasing in this interval. For all acquisitions during autumn 2011, the mean penetration into coniferous forest was higher than that into deciduous and mixed forest. The highest variation in SPC height and other statistics were observed in the time interval between the acquisitions on September 15 and October 18 which indicated that major leaf/needle drop and color change took place in this interval. For each time interval between consecutive acquisitions, the highest changes in the statistics were observed for the deciduous class which shows it is the most affected class by temporal variations (least for coniferous class). Results mentioned above were the same for HH and VV polarization modes. However, in all acquisitions and for each forest class, VV-pol mean SPC height and relevant location of SPC to the treetop were higher than HH-pol statistics and as expected, mean penetration depth

was highest for HH-pol acquisitions. Also, higher temporal variations in these statistics were observed for HH-pol data.

Coherence amplitude statistics, on the other hand, did not show dependence on the time during autumn. However, mean coherence of deciduous forest was always higher than coniferous and mixed classes. Coniferous forest mean coherence was found to be the lowest in all acquisitions and polarizations. Also, standard deviation of coherence was always highest for coniferous and lowest for the deciduous classes.

It has been found that it is possible to observe temporal variability of forest with X-band spaceborne interferometric radar of TanDEM-X mission. Dependencies of the coherence amplitude, SPC height, penetration depth and relevant SPC location statistics were successfully determined with respect to the forest classes. The results of the thesis mostly suited the theory and other research considering the interferometric coherence, SPC and penetration statistics. Specifically, in [19], it was demonstrated that coherence of deciduous forest is always higher than that for coniferous and mixed forest for a Finnish territory. In simulations [24], for stands with trees of the same height and number, mean penetration into coniferous stand was higher than that into deciduous stand. Theory [25], simulations [24] and the results obtained with some other TanDEM-X data [37] claimed that VV-pol signals are more attenuated than the HH-pol signals therefore resulting less penetration into the canopy.

The results about coherence amplitude statistics could not be explained with temporal dependencies since other factors were affecting the SAR system. Also, no straightforward relation is found between coherence amplitude and SPC statistics.

Some factors directly influenced the accuracy of our analysis. The most important of all was the accuracy and the resolution of the CLC2006 land cover database. In comparison to 2 x 2 meters resolution of radar data, the resolution of land cover map was 25 x 25 meters. Also, it has been stated that accuracy of forest classification was less than 70%. Second, there was almost a three year difference between radar and LIDAR acquisitions and a five year difference between radar and land cover data. In this period, forest is expected to grow and also some harvesting activities could be made. Third, radar data was affected by noise and therefore 15 x 15 averaging

window was applied for the interferometric coherence calculation. Finally, two-dimensional interpolation was applied to the radar data in order to fill the empty pixels which were originated from coordinate system transformation. However, the number of empty pixels was comparably small, so it is not expected to distort our results as much as other factors. Objectives of the thesis were focused on temporal changes in average values over a big test area, thus the aforementioned factors did not constitute a big problem for the analysis.

6.2 Future Work

Future work should consider the following suggestions:

- A land cover database with better accuracy and resolution should be used.
- Radar, reference and auxiliary data should be acquired on relatively close times.
- Height of ambiguity is defined as the altitude difference that generates an interferometric phase change of 2π radians after flat earth phase removal [31]. According to [36] the relative phase error from distributed scatterers is directly proportional to the height of ambiguity. The data used in this thesis have the height of ambiguity values between 170 and 302 meters. Higher baseline TanDEM-X data is required to reduce the height of ambiguity and therefore the noise in the final digital elevation model.
- Instead of transferring radar data into UTM coordinates, reference and auxiliary data can be transformed into radar slant range coordinates.

The results of the thesis indicate that there is a possible option to use the retrieved parameters and observed temporal variations in land cover classification since dependencies of those parameters on forest classes and also the temporal variations have shown distinct characteristics.

References

[1] M. Dobson, F. Ulaby, T. Le Toan, A. Beaudoin, E. Kasischke, and N. Christensen, "Dependence of radar backscatter on coniferous forest biomass," *IEEE Trans. Geosci. Remote Sens.*, vol. 30, no. 2, pp. 412–415, Mar. 1992.

[2] G. Smith and L.M.H. Ulander, "A model relating VHF-band backscatter to stem volume of coniferous boreal forest," *IEEE Trans. Geosci. Remote Sens.*, vol. 38 no. 2, pp. 728–740, Mar. 2000.

[3] M. Santoro, J. Askne, G. Smith, and J. E. S. Fransson, "Stem volume retrieval in boreal forests from ERS-1/2 interferometry," *Remote Sens. Environ.*, vol. 81, no. 1, pp. 19–35, 2002.

[4] M. Neumann, L. F. -Famil and A. Reigber, "Estimation of forest structure, ground and canopy layer characteristics from multi-baseline polarimetric interferometric SAR data," *IEEE Trans. Geosci. Remote Sens.*, vol. 48, no. 3, pp. 1086–1104, Mar. 2010.

[5] D. Zianis, P. Muukkonen, R. Mäkipää, and M. Manuccini, "Biomass and stem volume equations for tree species in Europe," *Silva Fennica Monographs*, vol. 4, pp. 1–63, 2005.

[6] T. Mette, K. P Papathanassiou, and I. Hajnsek, "Biomass estimation from polarimetric SAR interferometry over heterogeneous forest terrain," in *Proc. IEEE Int. Symp. Geosci. Remote Sensing (IGARSS'04)*, Anchorage, AK, pp. 511–514, Sep. 20–24, 2004.

[7] T. Mette, K. P. Papathanassiou, I. Hajnsek, H. Pretzsch, and P. Biber, "Applying a common allometric equation to convert forest height from Pol-InSAR data to forest biomass," in *Proc. IEEE Int. Symp. Geosci. Remote Sensing (IGARSS'04)*, Anchorage, AK, pp. 269–272, Sep. 20–24, 2004.

[8] M. Neumann, S. S. Saatchi, L. M. H. Ulander and J.E.S. Fransson, "Assessing performance of L- and P-band polarimetric interferometric SAR data in

estimating boreal forest above-ground biomass," *IEEE Trans. Geosci. Remote Sens*., vol. 50, no. 3, pp. 714–726, Mar. 2012.

[9] J. Praks, F. Kugler, K. P. Papathanassiou, I. Hajnsek, and M. Hallikainen, "Height estimation of boreal forest: Interferometric model-based inversion at L- and X-band versus HUTSCAT profiling scatterometer," *IEEE Trans. Geosci. Remote Sens*., vol. 4, no. 3, pp. 466–470, Jul. 2007.

[10] J. Praks, M. Hallikainen, J. Seppänen and J. Hyyppä, "Boreal forest height estimation with SAR interferometry and laser measurements," in *Proc. IEEE Int. Symp. Geosci. Remote Sensing (IGARSS'09)*, Cape Town, South Africa, pp. 308–311, Jul. 13–17, 2009.

[11] J. Praks, O. Antropov and M. Hallikainen, "LIDAR-aided SAR interferometry studies in boreal forest: scattering phase center and extinction coefficient at X- and L-Band," *IEEE Trans. Geosci. Remote Sens*., vol. 50, no. 10, pp. 3831–3843, Oct. 2012.

[12] F. Garestier, P. C. Dubois-Fernandez and K. P. Papathanassiou, "Pine forest height inversion using single-pass X-band PolInSAR data", *IEEE Trans. Geosci. Remote Sens*., vol. 46, no. 1, Jan. 2008.

[13] T. Aulinger, T. Mette, K. P. Papathanssiou, I. Hajnsek, M. Heurich, and P. Krzystek, "Validation of heights from interferometric SAR and LIDAR over the temperate forest site 'national park bayerischer wald'," in *Proc. 2nd Int. Workshop POLinSAR*, Frascati, Conference CD, Italy, Jan. 17–21, 2005.

[14] L. Ferro-Famil, E. Pottier, and J.-S. Lee, "Unsupervised classification of multifrequency and fully polarimetric SAR images based on the H/A/Alpha-Wishart classifier," *IEEE Trans. Geosci. Remote Sens.*, vol. 39, no. 11, pp. 2332–2342, Nov. 2001.

[15] C. Lardeux, P.-L. Frison, C. Tison, J.-C. Souyris, B. Stoll, B. Fruneau and J. -P. Rudant, "Support vector machine for multifrequency SAR polarimetric data classification," *IEEE Trans. Geosci. Remote Sens.*, vol. 47, no. 12, pp. 4143–4152, Dec. 2009.

[16] L. Loosvelt, J. Peters, H. Skriver, B. D. Baets and N. E. C. Verhoest, "Impact of reducing polarimetric SAR input on the uncertainty of crop classifications based on the random forests algorithm," *IEEE Trans. Geosci. Remote Sens.*, vol. 50, no. 10, pp. 4185–4200, Oct. 2012.

[17] Almeida-Filho, R., A. Rosenqvist, Y. E. Shimabukuro and R. Silva-Gomez, "Detecting deforestation with multitemporal L-band SAR imagery: A case study in western Brazilian Amazonia," *Int. J. Remote Sens.*, vol. 28, no. 6, pp. 1383–1390, 2007.

[18] F. Zhang, M. Xu, C. Xie, Z. Xia, K. Li, A. Cai, Y. Shao, X. Wang and R. Touzi, "Polarimetric signature and the temporal variation analysis for deforestation mapping in southwest China," in *Proc. Electromagnetics Research Symp.*, Suzhou, China, Sep. 2011.

[19] J. T. Koskinen, J. T. Pulliainen, M. Hyyppä, M. Engdahl, and M. T. Hallikainen, "The seasonal behavior of interferometric coherence in boreal forest," *IEEE Trans. Geosci. Remote Sens.*, vol. 39, pp. 820–829, Apr. 2001.

[20] J. Koskinen, J. Pulliainen, M. Mäkynen, and M. Hallikainen, "Seasonal comparison of HUTSCAT ranging scatterometer and ERS-1 SAR microwave signatures of Boreal forest zone," *IEEE Trans. Geosci. Remote Sens.*, vol. 37, pp. 2068–2080, July 1999.

[21] J. Pulliainen, L. Kurvonen, and M. Hallikainen, "Multi-temporal behavior of L- and C-band SAR observations of Boreal forests," *IEEE Trans. Geosci. Remote Sens.*, vol. 37, pp. 927–937, Mar. 1999.

[22] C. Proisy, E. Mougin, E. Dufrene, and V. le Dantec, "Monitoring seasonal changes of a mixed temperate forest using ERS-SAR observations," *IEEE Trans. Geosc. Remote Sens.*, vol. 38, pp. 540–552, Jan. 2000.

[23] P. C. D. Fernandez, T. L. Toan, S. Daniel, H. Oriot, J. Chave, L. Blanc, L. Villard, M. W. J. Davidson and M. Petit, "The TropiSAR airborne campaign in French Guiana: objectives, description, and observed temporal behavior of the backscatter signal," *IEEE Trans. Geosc. Remote Sens.*, vol. 50, no. 8, pp. 3228–3241, Aug. 2012.

[24] D. W. Liu, G. Q. Sun, W. Z. Yan and B.-I. Wu, "Analysis of InSAR sensitivity to forest structure based on radar scattering model," *Prog. Electromagnetics Research, PIERS* 84, pp. 149–171, 2008.

[25] H. Mott, "Remote sensing with polarimetric radar," John Wiley, New York, 2007.

[26] F. M. Henderson and A. J. Lewis, "Principles & applications of imaging radar," *Manual of Remote Sens.*, ed. 3, vol. 2, pp. 131–181, 1998.

[27] A. K. Fung and F.T. Ulaby, "Matter-energy interactions in the microwave region," *Manual of Remote Sens.*, ed. 2, vol. 1, pp. 115–164, 1983.

[28] L. E. B. Ericksson, "Satellite-borne L-band interferometric coherence for forestry applications in the boreal zone," Ph.D. dissertation, Friedrich-Schiller-University Jena, Jena, Germany, Jun. 2004.

[29] H. Hirosawa, Y. Matsuzaka, and O. Kobayashi, "Measurement of microwave backscatter from a cypress with and without leaves," *IEEE Trans. Geosc. Remote Sens.*, vol. 27, no. 6, pp. 698–701, Nov. 1989.

[30] J. O. Hagberg, L. M. H. Ulander and J. Askne, "Repeat-pass SAR interferometry over forested terrain," *IEEE Trans. Geosc. Remote Sens.*, vol. 33, no. 2, pp. 331–340, Mar. 1995.

[31] A. Ferretti, A. M. -Guarnieri, C. Prati and F. Rocca, "InSAR principles: guidelines for SAR interferometry processing and interpretation," *ESA Publications*, ESTEC, ISBN 92-9092-233-8, ISSN 1013–7076, The Netherlands, Feb. 2007.

[32] C. Wolff, "*Sythetic aperture radar*," [Online], Available: http://www.radartutorial.eu/20.airborne/ab07.en.html.

[33] J. Praks (Mar. 14, 2012), "*Radar and synthetic aperture radar – theory*," [Online]. Available: https://noppa.aalto.fi/noppa/kurssi/s-92.3132/luennot/S-92_3132_lecture_slides.pdf.

[34] ESA – European Space Agency (Oct. 22, 2012), "Radar and SAR Glossary," [Online], Available: http://envisat.esa.int/handbooks/asar/CNTR5-2.htm.

[35] T. Nagler, H. Rott, R. Hannsen, D. Moisseev, N. Adam, M. Eineder, B. Kampes, I. Hajnsek, K. P. Papathanassiou and S. R. Cloude, "The use of synthetic aperture radar (SAR) interferometry to retrieve bio- and geo-physical variables," Technical report, ENVEO, Innsbruck, Austria, Feb. 2004.

[36] G. Krieger, A. Moreira, H. Fiedler, I. Hajnsek, M. Werner, M. Younis, and M. Zink, "TanDEM-X: a satellite formation for high-resolution SAR interferometry", *IEEE Trans. Geosc. Remote Sens*., vol. 45, no. 11, pp. 3317–3341, Nov. 2007.

[37] F. Kugler, I. Hajnsek, and K. Papathanassiou, "Forest characterisation by means of TerraSAR-X and TanDEM-X polarimetric interferometric data," in *Proc. PolInSAR 5th Int. Workshop on Science and Applications of SAR Polarimetry and Polarimetric Interferometry*, Frascati, Italy, Jan. 24–28, 2011.

[38] F. Kugler, and I. Hajnsek, "Forest characterisation by means of TerraSAR-X and TanDEM-X (polarimetric and) interferometric data." in *Proc. IEEE Int. Symp. Geosci. Remote Sensing (IGARSS'11)*, Vancouver, Canada, pp. 2578–2581, Jul. 24–29, 2011.

[39] P. B. G. Dammert, "Spaceborne SAR interferometry: theory and applications", Ph.D. dissertation, Chalmers University of Technology, Göteborg, Sweden, 1999.

[40] M. A. Richards, "A beginner's guide to interferometric SAR concepts and signal processing," *IEEE Trans. Aerosp. Electron. Syst*., vol. 22, no. 9, pp. 5–29, Sep. 2007.

[41] Google Inc. (2009). Google Earth (Version 5.1.3533.1731) [Software]. Available: http://www.google.com/earth/download/ge//.

[42] CLC2000-Finland, Final Report, *Finnish Environment Institute*, May 2005.

[43] CLC2006 Finland, Final Technical Report, *Finnish Environment Institute*, Nov. 2009.

[44] DLR – Deutsches Zentrum fuer Luft- und Raumfahrt (German Aero-space Center), *TerraSAR-X – Germany's radar eye in space* [Online], Available: http://www.dlr.de/eo/en/desktopdefault.aspx/tabid-5725/9296_read-15979/.

[45] DLR – Deutsches Zentrum fuer Luft- und Raumfahrt (German Aero-space Center) (2009, July 8), *TerraSAR-X – Mission brochure* [Online], Available: http://www.dlr.de/eo/en/Portaldata/64/Resources/dokumente/TSX_brosch.pdf.

[46] DLR – Deutsches Zentrum fuer Luft- und Raumfahrt (German Aerospace Center) (2009, July 8), *TanDEM-X – A new high resolution interferometric SAR mission* [Online], Available: http://www.dlr.de/hr/desktopdefault.aspx/tabid-2317/3669_read-5488/.

[47] DLR – Deutsches Zentrum fuer Luft- und Raumfahrt (German Aero-space Center) (2009, July 8), *TanDEM-X – Mission brochure* [Online], Available: http://www.dlr.de/hr/Portaldata/32/Resources/dokumente/broschueren/TanDEM-X_web_Broschuere2010.pdf.

[48] T. Fritz, S. Duque, B. Bräutigam and J. L. B. Bello, "TanDEM-X ground segment – TanDEM-X experimental product description," *DLR Remote Sensing Technology Institute*, doc. TD-GS-PS-3028, issue 1.2, Jan. 2012.

[49] M. Sajana, "Estimation and mapping above ground woody carbon stocks using lidar data and digital camera imagery in the hilly forests of Gorkha, Nepal," M. Sc. thesis, University of Twente, Twente, The Netherlands, Feb. 2012.

[50] S. C. Popescu and R. H. Wayne, "Seeing the trees in forest: using lidar and multispectral data fusion with local filtering and variable window size for estimating tree height," in *Photogramm. Eng. Remote Sens.*, vol. 70, no. 5, pp. 589–604, May 2004.

[51] B. Delaunay, "Sur la sphère vide," *Izvestia Akademii Nauk SSSR, Otdelenie Matematicheskikh i Estestvennykh Nauk*, vol. 7, no. 6, pp. 793–800, 1934.

[52] Weather Underground, Inc. Available: http://www.wunderground.com/history/.

[53] Weather Underground (Weather Service), (2012, Aug. 10), Wikipedia, Available: http://en.wikipedia.org/wiki/Wunderground.

[54] D. M. Hurtado, "Interferometric processing of TanDEM-X images for forest height estimation," Final project, Aalto University, School of Electrical Engineering, Espoo, Finland, May 2012.

[55] W. Keydel, "Normal and differential SAR interferometry", Microwave and Radar Institute DLR, RTO-EN-SET-081, pp. 1–36, Oct. 2004.

[56] U. Balss, H. Breit, S. Duque, T. Fritz and C. Rossi, "TanDEM-X payload ground segment – CoSCC generation and interferometric considerations," *DLR Remote Sensing Technology Institute*, doc. TD-PGS-TN-3129, issue 1.0, May 2012.

[57] T. Kurkela, R. Drenkhan, M. Vuorinen, and M. Hanso, "Growth response of young Scots pines to needle loss assessed from productive foliage," *Metsanduslikud Uurimused / Forestry Studies*, vol. 50, pp. 5–22, 2009.

[58] K. Plattner, W. Volgger, W. Oberhuber, S. Mayr and H. Bauer, "Dry mass production in seedlings of Norway spruce infected by the needle rust Chrysomyxa rhododendri," *European Jour. of Forest Pathology*, vol. 29, pp. 365–370, 1999.